Measurement of the differential cross section of photon plus jet production in ppbar collisions at sqrts=1.96 TeV

V.M. Abazov, G. Sajot, J. Stark, S. Greder, F. Miconi, I. Ripp-Baudot, G. Bernardi, D. Brown, Y. Enari, J. Lellouch, et al.

FERMILAB-PUB-13-317-E

Measurement of the differential cross section of photon plus jet production in $p\bar{p}$ collisions at $\sqrt{s} = 1.96$ TeV

V.M. Abazov,[31] B. Abbott,[66] B.S. Acharya,[25] M. Adams,[45] T. Adams,[43] J.P. Agnew,[40] G.D. Alexeev,[31] G. Alkhazov,[35] A. Alton[a],[55] A. Askew,[43] S. Atkins,[53] K. Augsten,[7] C. Avila,[5] F. Badaud,[10] L. Bagby,[44] B. Baldin,[44] D.V. Bandurin,[43] S. Banerjee,[25] E. Barberis,[54] P. Baringer,[52] J.F. Bartlett,[44] U. Bassler,[15] V. Bazterra,[45] A. Bean,[52] M. Begalli,[2] L. Bellantoni,[44] S.B. Beri,[23] G. Bernardi,[14] R. Bernhard,[19] I. Bertram,[38] M. Besançon,[15] R. Beuselinck,[39] P.C. Bhat,[44] S. Bhatia,[57] V. Bhatnagar,[23] G. Blazey,[46] S. Blessing,[43] K. Bloom,[58] A. Boehnlein,[44] D. Boline,[63] E.E. Boos,[33] G. Borissov,[38] A. Brandt,[69] O. Brandt,[20] R. Brock,[56] A. Bross,[44] D. Brown,[14] X.B. Bu,[44] M. Buehler,[44] V. Buescher,[21] V. Bunichev,[33] S. Burdin[b],[38] C.P. Buszello,[37] E. Camacho-Pérez,[28] B.C.K. Casey,[44] H. Castilla-Valdez,[28] S. Caughron,[56] S. Chakrabarti,[63] K.M. Chan,[50] A. Chandra,[71] E. Chapon,[15] G. Chen,[52] S.W. Cho,[27] S. Choi,[27] B. Choudhary,[24] S. Cihangir,[44] D. Claes,[58] J. Clutter,[52] M. Cooke,[44] W.E. Cooper,[44] M. Corcoran,[71] F. Couderc,[15] M.-C. Cousinou,[12] D. Cutts,[68] A. Das,[41] G. Davies,[39] S.J. de Jong,[29,30] E. De La Cruz-Burelo,[28] F. Déliot,[15] R. Demina,[62] D. Denisov,[44] S.P. Denisov,[34] S. Desai,[44] C. Deterre[d],[20] K. DeVaughan,[58] H.T. Diehl,[44] M. Diesburg,[44] P.F. Ding,[40] A. Dominguez,[58] A. Dubey,[24] L.V. Dudko,[33] A. Duperrin,[12] S. Dutt,[23] M. Eads,[46] D. Edmunds,[56] J. Ellison,[42] V.D. Elvira,[44] Y. Enari,[14] H. Evans,[48] V.N. Evdokimov,[34] L. Feng,[46] T. Ferbel,[62] F. Fiedler,[21] F. Filthaut,[29,30] W. Fisher,[56] H.E. Fisk,[44] M. Fortner,[46] H. Fox,[38] S. Fuess,[44] A. Garcia-Bellido,[62] J.A. García-González,[28] V. Gavrilov,[32] W. Geng,[12,56] C.E. Gerber,[45] Y. Gershtein,[59] G. Ginther,[44,62] G. Golovanov,[31] P.D. Grannis,[63] S. Greder,[16] H. Greenlee,[44] G. Grenier,[17] Ph. Gris,[10] J.-F. Grivaz,[13] A. Grohsjean[c],[15] S. Grünendahl,[44] M.W. Grünewald,[26] T. Guillemin,[13] G. Gutierrez,[44] P. Gutierrez,[66] J. Haley,[54] L. Han,[4] K. Harder,[40] A. Harel,[62] J.M. Hauptman,[51] J. Hays,[39] T. Head,[40] T. Hebbeker,[18] D. Hedin,[46] H. Hegab,[67] A.P. Heinson,[42] U. Heintz,[68] C. Hensel,[20] I. Heredia-De La Cruz[d],[28] K. Herner,[44] G. Hesketh[f],[40] M.D. Hildreth,[50] R. Hirosky,[72] T. Hoang,[43] J.D. Hobbs,[63] B. Hoeneisen,[9] J. Hogan,[71] M. Hohlfeld,[21] J.L. Holzbauer,[57] I. Howley,[69] Z. Hubacek,[7,15] V. Hynek,[7] I. Iashvili,[61] Y. Ilchenko,[70] R. Illingworth,[44] A.S. Ito,[44] S. Jabeen,[68] M. Jaffré,[13] A. Jayasinghe,[66] M.S. Jeong,[27] R. Jesik,[39] P. Jiang,[4] K. Johns,[41] E. Johnson,[56] M. Johnson,[44] A. Jonckheere,[44] P. Jonsson,[39] J. Joshi,[42] A.W. Jung,[44] A. Juste,[36] E. Kajfasz,[12] D. Karmanov,[33] I. Katsanos,[58] R. Kehoe,[70] S. Kermiche,[12] N. Khalatyan,[44] A. Khanov,[67] A. Kharchilava,[61] Y.N. Kharzheev,[31] I. Kiselevich,[32] J.M. Kohli,[23] A.V. Kozelov,[34] J. Kraus,[57] A. Kumar,[61] A. Kupco,[8] T. Kurča,[17] V.A. Kuzmin,[33] S. Lammers,[48] P. Lebrun,[17] H.S. Lee,[27] S.W. Lee,[51] W.M. Lee,[43] X. Lei,[41] J. Lellouch,[14] D. Li,[14] H. Li,[72] L. Li,[42] Q.Z. Li,[44] J.K. Lim,[27] D. Lincoln,[44] J. Linnemann,[56] V.V. Lipaev,[34] R. Lipton,[44] H. Liu,[70] Y. Liu,[4] A. Lobodenko,[35] M. Lokajicek,[8] R. Lopes de Sa,[63] R. Luna-Garcia[g],[28] A.L. Lyon,[44] A.K.A. Maciel,[1] R. Madar,[19] R. Magaña-Villalba,[28] S. Malik,[58] V.L. Malyshev,[31] J. Mansour,[20] J. Martínez-Ortega,[28] R. McCarthy,[63] C.L. McGivern,[40] M.M. Meijer,[29,30] A. Melnitchouk,[44] D. Menezes,[46] P.G. Mercadante,[3] M. Merkin,[33] A. Meyer,[18] J. Meyer[i],[20] F. Miconi,[16] N.K. Mondal,[25] M. Mulhearn,[72] E. Nagy,[12] M. Narain,[68] R. Nayyar,[41] H.A. Neal,[55] J.P. Negret,[5] P. Neustroev,[35] H.T. Nguyen,[72] T. Nunnemann,[22] J. Orduna,[71] N. Osman,[12] J. Osta,[50] A. Pal,[69] N. Parashar,[49] V. Parihar,[68] S.K. Park,[27] R. Partridge[e],[68] N. Parua,[48] A. Patwa[j],[64] B. Penning,[44] M. Perfilov,[33] Y. Peters,[20] K. Petridis,[40] G. Petrillo,[62] P. Pétroff,[13] M.-A. Pleier,[64] V.M. Podstavkov,[44] A.V. Popov,[34] M. Prewitt,[71] D. Price,[48] N. Prokopenko,[34] J. Qian,[55] A. Quadt,[20] B. Quinn,[57] P.N. Ratoff,[38] I. Razumov,[34] I. Ripp-Baudot,[16] F. Rizatdinova,[67] M. Rominsky,[44] A. Ross,[38] C. Royon,[15] P. Rubinov,[44] R. Ruchti,[50] G. Sajot,[11] A. Sánchez-Hernández,[28] M.P. Sanders,[22] A.S. Santos[h],[1] G. Savage,[44] L. Sawyer,[53] T. Scanlon,[39] R.D. Schamberger,[63] Y. Scheglov,[35] H. Schellman,[47] C. Schwanenberger,[40] R. Schwienhorst,[56] J. Sekaric,[52] H. Severini,[66] E. Shabalina,[20] V. Shary,[15] S. Shaw,[56] A.A. Shchukin,[34] V. Simak,[7] N.B. Skachkov,[31] P. Skubic,[66] P. Slattery,[62] D. Smirnov,[50] G.R. Snow,[58] J. Snow,[65] S. Snyder,[64] S. Söldner-Rembold,[40] L. Sonnenschein,[18] K. Soustruznik,[6] J. Stark,[11] D.A. Stoyanova,[34] M. Strauss,[66] L. Suter,[40] P. Svoisky,[66] M. Titov,[15] V.V. Tokmenin,[31] Y.-T. Tsai,[62] D. Tsybychev,[63] B. Tuchming,[15] C. Tully,[60] L. Uvarov,[35] S. Uvarov,[35] S. Uzunyan,[46] R. Van Kooten,[48] W.M. van Leeuwen,[29] N. Varelas,[45] E.W. Varnes,[41] I.A. Vasilyev,[34] A.Y. Verkheev,[31] L.S. Vertogradov,[31] M. Verzocchi,[44] M. Vesterinen,[40] D. Vilanova,[15] P. Vokac,[7] H.D. Wahl,[43] M.H.L.S. Wang,[44] J. Warchol,[50] G. Watts,[73] M. Wayne,[50] J. Weichert,[21] L. Welty-Rieger,[47] M.R.J. Williams,[48] G.W. Wilson,[52] M. Wobisch,[53] D.R. Wood,[54] T.R. Wyatt,[40] Y. Xie,[44] R. Yamada,[44] S. Yang,[4] T. Yasuda,[44] Y.A. Yatsunenko,[31] W. Ye,[63] Z. Ye,[44] H. Yin,[44] K. Yip,[64] S.W. Youn,[44] J.M. Yu,[55]

J. Zennamo,[61] T.G. Zhao,[40] B. Zhou,[55] J. Zhu,[55] M. Zielinski,[62] D. Zieminska,[48] and L. Zivkovic[14]
(The D0 Collaboration*)

[1]*LAFEX, Centro Brasileiro de Pesquisas Físicas, Rio de Janeiro, Brazil*
[2]*Universidade do Estado do Rio de Janeiro, Rio de Janeiro, Brazil*
[3]*Universidade Federal do ABC, Santo André, Brazil*
[4]*University of Science and Technology of China, Hefei, People's Republic of China*
[5]*Universidad de los Andes, Bogotá, Colombia*
[6]*Charles University, Faculty of Mathematics and Physics, Center for Particle Physics, Prague, Czech Republic*
[7]*Czech Technical University in Prague, Prague, Czech Republic*
[8]*Institute of Physics, Academy of Sciences of the Czech Republic, Prague, Czech Republic*
[9]*Universidad San Francisco de Quito, Quito, Ecuador*
[10]*LPC, Université Blaise Pascal, CNRS/IN2P3, Clermont, France*
[11]*LPSC, Université Joseph Fourier Grenoble 1, CNRS/IN2P3, Institut National Polytechnique de Grenoble, Grenoble, France*
[12]*CPPM, Aix-Marseille Université, CNRS/IN2P3, Marseille, France*
[13]*LAL, Université Paris-Sud, CNRS/IN2P3, Orsay, France*
[14]*LPNHE, Universités Paris VI and VII, CNRS/IN2P3, Paris, France*
[15]*CEA, Irfu, SPP, Saclay, France*
[16]*IPHC, Université de Strasbourg, CNRS/IN2P3, Strasbourg, France*
[17]*IPNL, Université Lyon 1, CNRS/IN2P3, Villeurbanne, France and Université de Lyon, Lyon, France*
[18]*III. Physikalisches Institut A, RWTH Aachen University, Aachen, Germany*
[19]*Physikalisches Institut, Universität Freiburg, Freiburg, Germany*
[20]*II. Physikalisches Institut, Georg-August-Universität Göttingen, Göttingen, Germany*
[21]*Institut für Physik, Universität Mainz, Mainz, Germany*
[22]*Ludwig-Maximilians-Universität München, München, Germany*
[23]*Panjab University, Chandigarh, India*
[24]*Delhi University, Delhi, India*
[25]*Tata Institute of Fundamental Research, Mumbai, India*
[26]*University College Dublin, Dublin, Ireland*
[27]*Korea Detector Laboratory, Korea University, Seoul, Korea*
[28]*CINVESTAV, Mexico City, Mexico*
[29]*Nikhef, Science Park, Amsterdam, the Netherlands*
[30]*Radboud University Nijmegen, Nijmegen, the Netherlands*
[31]*Joint Institute for Nuclear Research, Dubna, Russia*
[32]*Institute for Theoretical and Experimental Physics, Moscow, Russia*
[33]*Moscow State University, Moscow, Russia*
[34]*Institute for High Energy Physics, Protvino, Russia*
[35]*Petersburg Nuclear Physics Institute, St. Petersburg, Russia*
[36]*Institució Catalana de Recerca i Estudis Avançats (ICREA) and Institut de Física d'Altes Energies (IFAE), Barcelona, Spain*
[37]*Uppsala University, Uppsala, Sweden*
[38]*Lancaster University, Lancaster LA1 4YB, United Kingdom*
[39]*Imperial College London, London SW7 2AZ, United Kingdom*
[40]*The University of Manchester, Manchester M13 9PL, United Kingdom*
[41]*University of Arizona, Tucson, Arizona 85721, USA*
[42]*University of California Riverside, Riverside, California 92521, USA*
[43]*Florida State University, Tallahassee, Florida 32306, USA*
[44]*Fermi National Accelerator Laboratory, Batavia, Illinois 60510, USA*
[45]*University of Illinois at Chicago, Chicago, Illinois 60607, USA*
[46]*Northern Illinois University, DeKalb, Illinois 60115, USA*
[47]*Northwestern University, Evanston, Illinois 60208, USA*
[48]*Indiana University, Bloomington, Indiana 47405, USA*
[49]*Purdue University Calumet, Hammond, Indiana 46323, USA*
[50]*University of Notre Dame, Notre Dame, Indiana 46556, USA*
[51]*Iowa State University, Ames, Iowa 50011, USA*
[52]*University of Kansas, Lawrence, Kansas 66045, USA*
[53]*Louisiana Tech University, Ruston, Louisiana 71272, USA*
[54]*Northeastern University, Boston, Massachusetts 02115, USA*
[55]*University of Michigan, Ann Arbor, Michigan 48109, USA*
[56]*Michigan State University, East Lansing, Michigan 48824, USA*
[57]*University of Mississippi, University, Mississippi 38677, USA*
[58]*University of Nebraska, Lincoln, Nebraska 68588, USA*
[59]*Rutgers University, Piscataway, New Jersey 08855, USA*

[60]Princeton University, Princeton, New Jersey 08544, USA
[61]State University of New York, Buffalo, New York 14260, USA
[62]University of Rochester, Rochester, New York 14627, USA
[63]State University of New York, Stony Brook, New York 11794, USA
[64]Brookhaven National Laboratory, Upton, New York 11973, USA
[65]Langston University, Langston, Oklahoma 73050, USA
[66]University of Oklahoma, Norman, Oklahoma 73019, USA
[67]Oklahoma State University, Stillwater, Oklahoma 74078, USA
[68]Brown University, Providence, Rhode Island 02912, USA
[69]University of Texas, Arlington, Texas 76019, USA
[70]Southern Methodist University, Dallas, Texas 75275, USA
[71]Rice University, Houston, Texas 77005, USA
[72]University of Virginia, Charlottesville, Virginia 22904, USA
[73]University of Washington, Seattle, Washington 98195, USA

(Dated: August 12, 2013)

We study the process of associated photon and jet production, $p\bar{p} \to \gamma + \text{jet} + X$, using 8.7 fb^{-1} of integrated luminosity collected by the D0 detector at the Fermilab Tevatron Collider at a center-of-mass energy $\sqrt{s} = 1.96$ TeV. Photons are reconstructed with rapidity $|y^\gamma| < 1.0$ or $1.5 < |y^\gamma| < 2.5$ and transverse momentum $p_T^\gamma > 20$ GeV. The highest-p_T jet is required to be in one of four rapidity regions up to $|y^{\text{jet}}| \leq 3.2$. For each rapidity configuration we measure the differential cross sections in p_T^γ separately for events with the same sign ($y^\gamma y^{\text{jet}} > 0$) and opposite sign ($y^\gamma y^{\text{jet}} \leq 0$) of photon and jet rapidities. We compare the measured triple differential cross sections, $\mathrm{d}^3\sigma/\mathrm{d}p_T^\gamma \mathrm{d}y^\gamma \mathrm{d}y^{\text{jet}}$, to next-to-leading order (NLO) perturbative QCD calculations using different sets of parton distribution functions and to predictions from the SHERPA and PYTHIA Monte Carlo event generators. The NLO calculations are found to be in general agreement with the data, but do not describe all kinematic regions.

PACS numbers: 13.85.Qk, 12.38.Qk

I. INTRODUCTION

In hadron-hadron collisions, high-energy photons (γ) emerge unaltered from the hard scattering process of two partons and therefore provide a clean probe of the parton dynamics. The study of such photons (called *prompt*) produced in association with a jet can be used to extend inclusive photon production measurements [1–6] and provide information about the parton distribution functions (PDFs) of the incoming hadrons [7–13]. The term "prompt" means that these photons do not result from mesons, for example, π^0, η, ω, or K_S^0 decays. Such events are mostly produced in Quantum Chromodynamics (QCD) directly through the Compton-like scattering process $gq \to \gamma q$ and through quark-antiquark annihilation $q\bar{q} \to \gamma g$. Inclusive γ+jet production may also originate from partonic processes such as $gg \to q\bar{q}$, $qg \to qg$, or $qq \to qq$ where a final state quark or gluon produces a photon during fragmentation (fragmentation photon) [8, 14], and another parton fragments into a jet. Photon isolation requirements substantially reduce the rates of these events. However, their contribution is still noticeable in some regions of phase space, for example, at low photon transverse momentum, p_T^γ.

By selecting events with different angular configurations between the photon and the jets, the data probe different ranges of parton momentum fraction x and hard-scattering scales Q^2, as well as providing some differentiation between contributing partonic subprocesses.

In this article, we present an analysis of γ+jet production in $p\bar{p}$ collisions at a center-of-mass energy $\sqrt{s} = 1.96$ TeV in which the highest-p_T (leading) photon is produced either centrally with a rapidity $|y^\gamma| < 1.0$ or in the forward rapidity region with $1.5 < |y^\gamma| < 2.5$ [15]. The leading jet is required to be in one of the four rapidity regions, $|y^{\text{jet}}| \leq 0.8$, $0.8 < |y^{\text{jet}}| \leq 1.6$, $1.6 < |y^{\text{jet}}| \leq 2.4$, or $2.4 < |y^{\text{jet}}| \leq 3.2$, and to satisfy the minimum transverse momentum requirement $p_T^{\text{jet}} > 15$ GeV. The cross section as a function of p_T^γ is measured differentially for sixteen angular configurations of the leading jet and the photon rapidities. These configurations are obtained by combining the two photon and four jet rapidity regions, considered separately for events having the same sign and opposite sign of photon and jet rapidities, i.e. $y^\gamma y^{\text{jet}} > 0$ and $y^\gamma y^{\text{jet}} \leq 0$.

The primary motivation of this measurement is to constrain the gluon PDF that directly affects the rate of Compton-like $qg \to q\gamma$ parton scattering. The rate of this process varies for different photon-jet rapidity configurations and drops with increasing p_T^γ. Estimates us-

*with visitors from [a]Augustana College, Sioux Falls, SD, USA, [b]The University of Liverpool, Liverpool, UK, [c]DESY, Hamburg, Germany, [d]Universidad Michoacana de San Nicolas de Hidalgo, Morelia, Mexico [e]SLAC, Menlo Park, CA, USA, [f]University College London, London, UK, [g]Centro de Investigacion en Computacion - IPN, Mexico City, Mexico, [h]Universidade Estadual Paulista, São Paulo, Brazil, [i]Karlsruher Institut für Technologie (KIT) - Steinbuch Centre for Computing (SCC) and [j]Office of Science, U.S. Department of Energy, Washington, D.C. 20585, USA.

ing the PYTHIA [16] Monte Carlo (MC) event generator and CTEQ6L PDF set [17] show that the highest fraction of qg events is observed in same-sign events with forward photons ($y^{\gamma}y^{\rm jet}>0$ and $1.5<|y^{\gamma}|<2.5$). Figure 1 shows the expected contributions of the Compton-like process to the total associated production cross section of a photon and a jet for the four jet rapidity intervals in same-sign events with forward photons. In these events the qg fraction increases with jet rapidity.

The PDFs entering the theoretical predictions have substantial uncertainties, particularly for the gluon contributions at small x, or large x and large Q^2 [17]. The $\gamma+$jet cross sections probe different regions of parton momentum fraction x_1 and x_2 of the two initial interacting partons. For example, at $p_T^{\gamma}\approx 20-25$ GeV, events with a central photon and central jet cover the interval in $0.01<x<0.06$, while same-sign events with a forward photon and very forward jet ($2.4<|y^{\rm jet}|\leq 3.2$) cover the regions within $0.001<x<0.004$ and $0.2<x<0.5$. Here, x is defined using the leading-order approximation $x_{1,2}=(p_T^{\gamma}/\sqrt{s})(\exp(\pm y^{\gamma})+\exp(\pm y^{\rm jet}))$ [8]. The total x and Q^2 region (with Q^2 taken as $(p_T^{\gamma})^2$) covered by the measurement is $0.001\leq x\leq 1$ and $400\leq Q^2\leq 1.6\times 10^5$ GeV^2, extending the kinematic reach of previous $\gamma+$jet measurements [18–26].

The expected ratio of the direct photon contribution to the sum of direct and fragmentation contributions of the $\gamma+$jet cross section is shown in Fig. 2, for the chosen photon isolation criteria (see Sec. II B), in the four studied regions. The fragmentation contribution decreases with increasing p_T^{γ} for all regions [14, 27, 28].

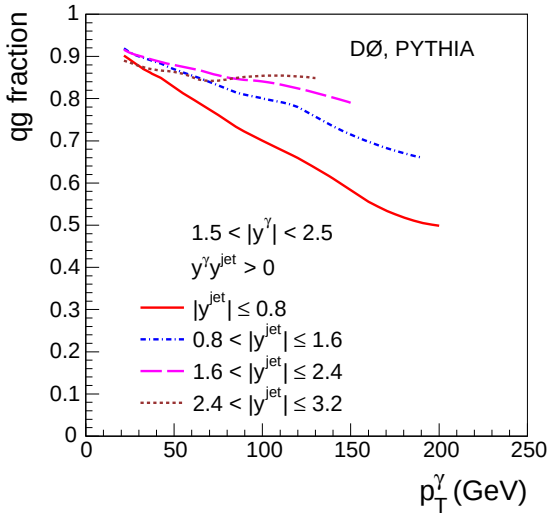

FIG. 1: (color online) The fraction of events, estimated using the PYTHIA event generator [16] with CTEQ6L PDF set [17], produced via the $qg\rightarrow q\gamma$ subprocess relative to the total cross section of associated production of a direct photon in the forward rapidity region, $1.5<|y^{\gamma}|<2.5$, and a leading jet in one of the four rapidity intervals satisfying $y^{\gamma}y^{\rm jet}>0$.

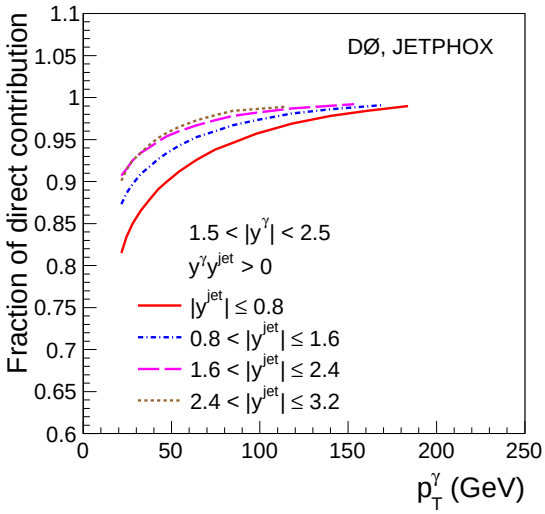

FIG. 2: (color online) For $\gamma+$jet events, the fraction of the direct (non-fragmentation) photon contribution of the total (direct+fragmentation) cross section, estimated with JETPHOX [29] for events with forward photons.

Compared to the latest $\gamma+$jet cross sections published by the D0 [25] and ATLAS [26] Collaborations, this measurement considers not only central but also forward photon rapidities, four jet rapidity intervals, and uses a significantly larger data set.

This paper is organized as follows. In Sec. II, we briefly describe the D0 detector and $\gamma+$jet events selection criteria. In Sec. III, we describe the MC signal and background samples used in the analysis. In Sec. IV, we assess the main corrections applied to the data needed to measure the cross sections and discuss related uncertainties in Sec. V. Measured cross sections and comparisons with theoretical predictions are presented in Sec. VI. Finally, Sec. VII summarizes the results.

II. D0 DETECTOR AND DATA SET

A. D0 detector

The D0 detector is a general purpose detector described in detail elsewhere [30–32]. The subdetectors most relevant in this analysis are the calorimeter, the central tracking system, and the central preshower. The muon detection system is used for selecting a clean $Z\rightarrow\mu^+\mu^-\gamma$ sample to obtain data-to-MC correction factors for the photon reconstruction efficiency. The central tracking system, used to reconstruct tracks of charged particles, consists of a silicon micro-strip detector (SMT) and a central fiber track detector (CFT), both inside a 2 T solenoidal magnetic field. While the amount of material traversed by a charged particle depends on its trajectory, it is typically on the order of 0.1 radiation lengths

in the tracking system. The tracking system provides a 35 μm vertex resolution along the beam line and 15 μm resolution in the transverse plane near the beam line for charged particles with $p_T \approx 10$ GeV. The solenoid magnet is surrounded by the central preshower (CPS) detector located immediately before the inner layer of the electromagnetic calorimeter. The CPS consists of approximately one radiation length of lead absorber surrounded by three layers of scintillating strips. The preshower detectors are in turn surrounded by sampling calorimeters constructed of depleted uranium absorbers in an active liquid argon volume. The calorimeter is composed of three sections: a central calorimeter (CC) covering the range of pseudorapidities $|\eta_{\rm det}| < 1.1$ [15] and two end calorimeters (EC) with coverage extending to $|\eta_{\rm det}| \approx 4.2$, with all three housed in separate cryostats. The electromagnetic (EM) section of the central calorimeter contains four longitudinal layers of approximately 2, 2, 7, and 10 radiation lengths, and is finely-segmented transversely into cells of size $\Delta\eta_{\rm det} \times \Delta\phi_{\rm det} = 0.1 \times 0.1$, with the exception of layer three with 0.05×0.05 granularity. The calorimeter resolution for measurements of the electron/photon energy at 50 GeV is about 3.6%. The luminosity is measured using plastic scintillator arrays placed in front of the EC cryostats at $2.7 < |\eta_{\rm det}| < 4.4$.

B. Event selection

Triggers for the events used for this analysis are based on at least one cluster of energy found in the EM calorimeter with loose shower shape requirement and various p_T^γ thresholds. The data set with photon candidates covering the interval of $20 < p_T^\gamma \leq 35$ GeV is selected using prescaled EM triggers with a p_T threshold of 17 GeV and corresponds to a total integrated luminosity of 7.00 ± 0.43 pb^{-1}. The selection efficiency of photons with respect to this trigger condition exceeds 96%. As a cross check, the cross sections in this p_T^γ region are also measured using events that are heavily prescaled with trigger thresholds of $p_T = 13$ GeV or 9 GeV corresponding to total luminosities of 2.63 ± 0.16 pb^{-1} and 0.65 ± 0.04 pb^{-1}, respectively [33].

Photon candidates with $p_T > 35$ GeV are selected using a set of unprescaled EM triggers with p_T thresholds between 20 GeV and 70 GeV, with a signal selection efficiency with respect to the trigger requirements close to 100%. This data set corresponds to an integrated luminosity of 8.7 ± 0.5 fb^{-1} [33] after relevant data quality cuts.

The D0 tracking system is used to select events containing at least one $p\bar{p}$ collision vertex reconstructed with at least three tracks and within 60 cm of the center of the detector along the beam axis. The efficiency of the vertex requirements above varies as a function of instantaneous luminosity within $95\% - 97\%$.

The longitudinal segmentation of the EM calorimeter and CPS detector allows the estimation of the direction of the central photon candidate and the coordinate of its origin along the beam axis ("photon vertex pointing"). This position is required to be within 10 cm (3 standard deviations) of the $p\bar{p}$ collision vertex if there is a CPS cluster matched to the photon EM cluster ($\sim 80\%$ of events) or within 32 cm otherwise (about 1.5 standard deviation for such events). Forward photons are assumed to originate from the default $p\bar{p}$ collision vertex. A systematic uncertainty is assigned to account for this assumption.

C. Photon and jet selections

EM clusters for photon candidates are formed from calorimeter towers in a cone of radius $\mathcal{R} = \sqrt{(\Delta\eta)^2 + (\Delta\phi)^2} = 0.4$ around a seed tower [30]. A stable cone is found iteratively, and the final cluster energy is recalculated from an inner cone within $\mathcal{R} = 0.2$. The photon candidates are required (i) to have $\geq 97\%$ of the cluster energy deposited in the EM calorimeter layers; (ii) to be isolated in the calorimeter with $\mathcal{I} = [E_{\rm tot}(0.4) - E_{\rm EM}(0.2)]/E_{\rm EM}(0.2) < 0.07$, where $E_{\rm tot}(\mathcal{R})$ $[E_{\rm EM}(\mathcal{R})]$ is the total [EM only] energy in a cone of radius $\mathcal{R}$; (iii) to have a scalar sum of the p_T of all charged particles originating from the vertex in an annulus of $0.05 < \mathcal{R} < 0.4$ around the EM cluster to be less than 1.5 GeV; and (iv) to have an energy-weighted EM shower width consistent with that expected for a photon. To suppress electrons misidentified as photons, the EM clusters are required to have no spatial match to a charged particle track or any hit configuration in the SMT and CFT detectors consistent with an electron trajectory [34]. This requirement is referred to as a "track-match veto".

An additional group of variables exploiting the differences between the photon- and jet-initiated activity in the EM calorimeter, CPS (for central photons), and the tracker is combined into an artificial neural network (NN) to further reject jet background [35]. In these background events, photons are mainly produced from decays of energetic π^0 and η mesons. The NN is trained on a PYTHIA [16] MC sample of photon and jets events. The generated MC events are processed through a GEANT-based simulation of the D0 detector [36]. Simulated events are overlaid with data events from random $p\bar{p}$ crossings to properly model the effects of multiple $p\bar{p}$ interactions and detector noise in data. Care is taken to ensure that the instantaneous luminosity distribution in the overlay events is similar to the data used in the analysis. MC events are then processed through the same reconstruction procedure as the data. They are weighted to take into account the trigger efficiency in data, and small observed differences in the distributions of the instantaneous luminosity and of the z coordinate of the $p\bar{p}$ collision vertex. Photons radiated from charged leptons in Z boson decays ($Z \to \ell^+\ell^-\gamma$, $\ell = e, \mu$) are used to validate the NN performance [37–39]. The shape of

the NN output ($O_{\rm NN}$) distribution in the MC simulation describes the data well and gives an additional discrimination against jets. The $O_{\rm NN}$ distribution for jets is validated using dijet MC and data samples enriched in jets misidentified as photons. For this purpose, the jets are required to pass all photon identification criteria listed above, but with an inverted calorimeter isolation requirement of $\mathcal{I} > 0.1$ or by requiring at least one track in a cone of $\mathcal{R} < 0.05$ around the photon candidate. The photon candidates are selected with a requirement $O_{\rm NN} > 0.3$ to retain $97\% - 98\%$ of photons and to reject $\approx 40\%$ ($\approx 15\%$) of jets remaining after the other selections described above for central (forward) photons have been applied.

Background contributions from cosmic rays and from isolated electrons, originating from the leptonic decays of W bosons, are suppressed by requiring the missing transverse energy $\not\!\!E_T$, calculated as a vector sum of the transverse energies of all calorimeter cells and corrected for reconstructed objects (photon and jet energy scale corrections), to satisfy the condition $\not\!\!E_T < 0.7\ p_T^\gamma$.

The measured energy of a photon EM cluster is calibrated in two steps. First, the absolute energy calibration of the EM cluster is obtained using electrons from $Z \to e^+e^-$ decays as a function of $\eta_{\rm det}$ and p_T. However, photons interact less with the material in front of the calorimeter than electrons. As a result the electron energy scale correction overestimates the photon p_T relative to the particle (true) level. The relative photon energy correction as a function of η is derived using a detailed GEANT-based [36] simulation of the D0 detector response. It is particularly sizable at low p_T ($p_T^\gamma \approx 20$ GeV), where the photon energy overcorrection is found to be $\approx 3\%$. The difference between electron and photon calibrations becomes smaller at higher energies. A systematic uncertainty of $0.60\% - 0.75\%$ on this correction is due to the electron energy calibration and uncertainties in the description of the amount of material in front of the calorimeter. Combined with the steeply falling p_T^γ spectrum this results in a $3\% - 5\%$ uncertainty on the measured cross sections (see Section V).

Selected events should contain at least one hadronic jet. Jets are reconstructed using the D0 Run II Midpoint Cone jet-finding algorithm with a cone of $\mathcal{R} = 0.7$ [40], and are required to satisfy quality criteria that suppress backgrounds from leptons, photons, and detector noise effects. Jet energies are corrected to the particle level using a jet energy scale correction procedure [41]. The leading jet must satisfy two requirements: $p_T^{\rm jet} > 15$ GeV and $p_T^{\rm jet} > 0.3 p_T^\gamma$, where the first is related with the jet p_T reconstruction threshold of 6 GeV for the uncorrected jet p_T. The second requirement reflects the correlation between photon and leading jet p_T, and is optimized at the reconstruction level to account for jet p_T resolution. At the particle level, this selection reduces the fraction of events with strong radiation in the initial or/and final state which potentially may lead to higher order corrections in theory, i.e., uncertainty to the current *NLO* QCD predictions. The jet p_T selections above have about $90\% - 95\%$ efficiency for the signal. The leading photon candidate and the leading jet are also required to be separated in η-ϕ space by $\Delta\mathcal{R}(\gamma, {\rm jet}) > 0.9$.

In total, approximately 7.2 (8.3) million γ + jet candidate events with central (forward) photons are selected after application of all selection criteria.

III. SIGNAL AND BACKGROUND MODELS

To study the characteristics of signal events, MC samples are generated using PYTHIA [16] and SHERPA [42] event generators, with CTEQ6.1L and CTEQ6.6M PDF sets [17], respectively. In PYTHIA, the signal events are included via $2 \to 2$ matrix elements (ME) with $gq \to \gamma q$ and $q\bar{q} \to \gamma g$ hard scatterings (defined at the leading order) followed by the leading-logarithm approximation of the partonic shower. The soft underlying events, as well as fragmentation, are based on an empirical model ("Tune A"), tuned to Tevatron data [43].

In SHERPA, up to two extra partons (and thus jets) are allowed at the ME level in the $2 \to \{2, 3, 4\}$ scattering, but jets can also be produced in parton showers (PS). Matching between partons coming from real emissions in the ME and jets from PS is done at an energy scale $Q_{\rm cut}$ defined following the prescriptions given in Ref. [44]. Compared with Tune A the multiple parton interaction (MPI) model implemented in SHERPA is characterized by (a) showering effects in the second interaction, which makes it closer to the p_T-ordered showers [45] in the Perugia tunes [46], and (b) a combination of the CKKW merging approach with the MPI modeling [42, 47]. Another distinctive feature of SHERPA is the modeling of the parton-to-photon fragmentation contributions through the incorporation of QED effects into the parton shower [44]. This contribution is available in SHERPA with default settings for γ + jet events.

Since we measure the cross section of *isolated* prompt photons, the isolation criterion should be defined in the MC sample as well to allow a comparison of data to expectations. In the PYTHIA and SHERPA samples, the photon is required to be isolated at the particle level by $p_T^{\rm iso} = p_T^{\rm tot}(0.4) - p_T^\gamma < 2.5$ GeV, where $p_T^{\rm tot}(0.4)$ is the total transverse energy of particles within a cone of radius $\mathcal{R} = 0.4$ centered on the photon. Here, the particle level includes all stable particles as defined in Ref. [48]. The photon isolation at the particle level differs from that at the reconstruction level (see Sec. II C), and includes specific requirements on the calorimeter isolation (defined around the EM cluster) and track isolation.

To estimate backgrounds to γ + jet production, we also consider dijet events simulated in PYTHIA. In the latter, constraints are placed at the generator level to increase the number of jet events fluctuating into photon-like objects [35] after applying photon selection criteria. The signal events may contain photons originating from the parton-to-photon fragmentation process.

For this reason, the background events, produced with QCD processes in PYTHIA, were preselected to exclude bremsstrahlung photons produced from partons. Finally, to estimate other possible backgrounds, we have also used W+jet and Z+jet samples simulated with ALPGEN+PYTHIA [49], and diphoton events simulated with SHERPA. Signal and background events are processed through a GEANT-based [36] simulation and event reconstruction as described in the previous section.

IV. DATA ANALYSIS AND CORRECTIONS

A. Estimating signal fraction

Two types of instrumental background contaminate the γ+jet sample: electroweak interactions resulting in one or more electromagnetic clusters (from electrons or photons), and strong interactions producing a jet misidentified as a photon.

The first type of background includes $W(\rightarrow e\nu)$+jet, $Z/\gamma^*(\rightarrow e^+e^-)$+jet, and diphoton production. The contributions from these backgrounds are estimated from MC simulation. In the case of $W(\rightarrow e\nu)$+jet events, with the electron misidentified as a photon, the neutrino will contribute additional $\not\!\!E_T$. The combination of the track-match veto (part of the photon identification criteria), and $\not\!\!E_T$ requirement reduces the contribution from this process to a negligible level, less than 0.5% for events with central photons, and less than 1.5% for events with forward photons. Contributions from Z+jet and diphoton events, in which either $e^{\pm}$ from Z decay is misidentified as a photon, or one of the photons in the diphoton events is misidentified as a jet, are found to be even smaller. These backgrounds are subtracted from the selected data sample.

To estimate the remaining background contribution from dijet events, we consider photon candidates in the region $0.3 < O_{\rm NN} \leq 1$ (i.e. the region used for data analysis). The distributions for the simulated photon signal and dijet background samples are fitted to the data for each p_T^γ bin using a maximum likelihood fit [50] to obtain the fractions of signal and background components in data. The result of this fit to $O_{\rm NN}$ templates, normalized to the number of events in data, is shown in Fig. 3 for central photons with $50 < p_T^\gamma < 60$ GeV, as an example. The p_T^γ dependence of the signal fraction (purity) is fitted in each region using a three-parameter function, $\mathcal{P} = a/(1 + b(p_T^\gamma)^c)$. Two alternative fitting functions have also been considered. Figure 4 shows the resulting purities for events with central photons, very central and very forward jet rapidities, for same-sign and opposite-sign rapidities. Figure 5 shows similar results for events with forward photons. The signal fractions, typically, grow with p_T^γ, while the growth is not as significant for the events with forward photons. The signal fractions are somewhat greater for the same-sign rapidity events than for the opposite-sign, and also greater for events with central jets as opposed to forward jet events.

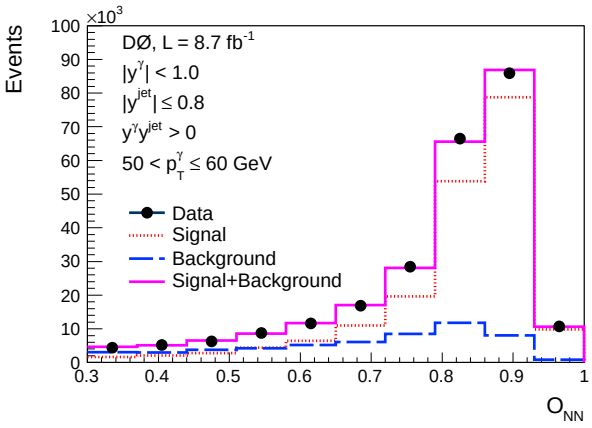

FIG. 3: (color online) Distribution of observed events for $O_{\rm NN}$ after all selection criteria for the representative bin $50 < p_T^\gamma < 60$ GeV ($|y^\gamma| < 1.0$). The distributions for the signal and background templates are shown normalized to their respective fitted fractions. Fits in the other p_T^γ bins are of similar quality.

The measured fractions of signal events have to be corrected for events with prompt photons with the isolation parameter value at the particle level $p_T^{\rm iso} \geq 2.5$ GeV. Such events can migrate into our data sample even after applying the photon selections described in Sec. II C. The fractions of such events are estimated in two ways. First, we use the signal models in SHERPA and PYTHIA MC generators to determine the fraction of events with $p_T^{\rm iso} \geq 2.5$ GeV after all selections. The fraction of such events is $1\% - 3\%$ for events with central photons and $1\% - 2\%$ for events with forward photons. This procedure gives consistent results for both MC generators. In the second method, we calculate signal purities for the signal events in which we keep *all* photons, i.e., including those with isolation $p_T^{\rm iso} \geq 2.5$ GeV, and compare them with the default case where photons satisfy the isolation cut $p_T^{\rm iso} < 2.5$. The difference of $1\% - 3\%$ is in good agreement with the direct MC estimates. We subtract this fraction from data and assign an additional systematic uncertainty on the signal purity of $1\% - 1.5\%$.

Other systematic uncertainties on the signal purity are caused by the $O_{\rm NN}$ template fitting uncertainties derived from the error matrix, the choice of fit functions, and the signal model dependence estimated by a comparison of signal purities obtained with the photon templates taken from PYTHIA and SHERPA. An additional systematic uncertainty on the background template due to the fragmentation model implemented in PYTHIA is also taken into account. It is found to be about 5% at $p_T^\gamma \simeq 30$ GeV, 2% at $p_T^\gamma \simeq 50$ GeV, and 1% at $p_T^\gamma \gtrsim 70$ GeV and is estimated using the method described in Ref. [4].

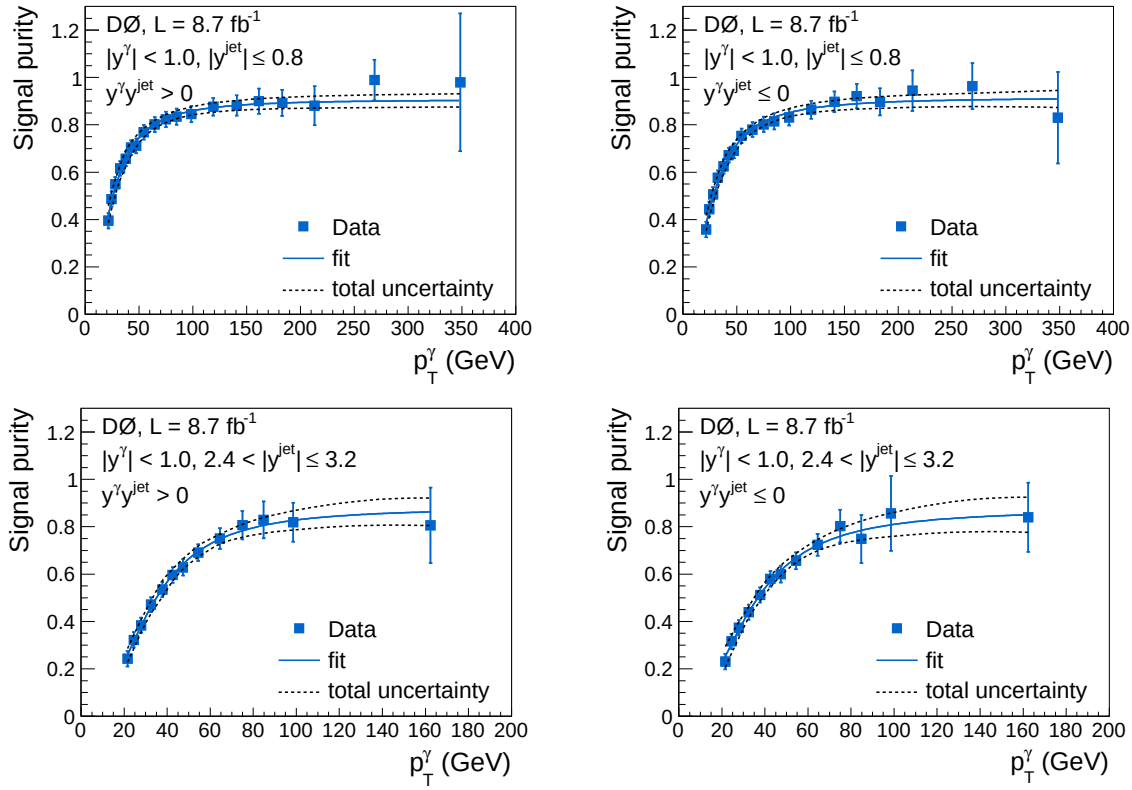

FIG. 4: (color online) Purity of the selected γ + jet sample as a function of p_T^γ, shown for central photons, very central and very forward jet rapidities, same-sign, and opposite-sign rapidity events. The solid line shows the fit and the dashed lines show the total fit uncertainty.

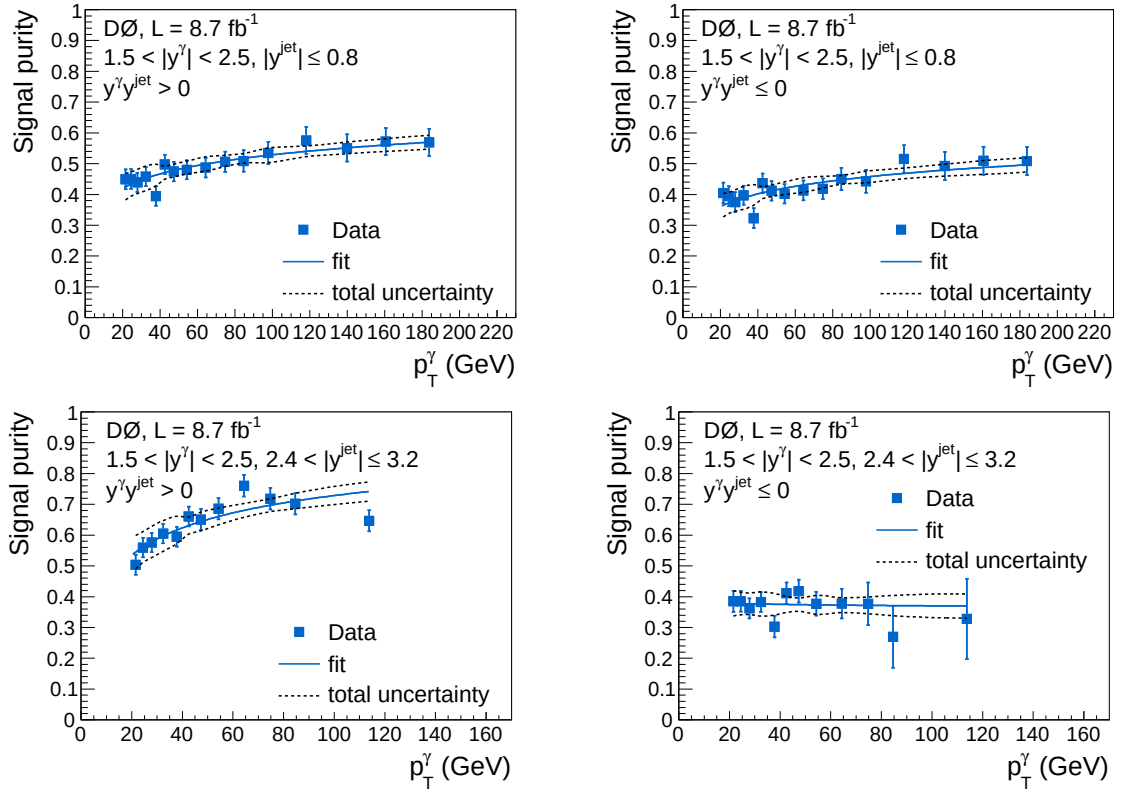

FIG. 5: (color online) Same as Fig. 4 but for events with forward photons.

B. Acceptance and efficiency corrections

We calculate corrections to the observed rate of $\gamma+$jet candidates to account for the photon and jet detection efficiencies (and for the geometric and kinematic acceptances) using samples of simulated γ+jet events in which the photon is required to be isolated at the particle level by applying $p_T^{\rm iso} < 2.5$ GeV.

The bin size is chosen to be larger than the resolution on p_T^γ, yielding more than 80% of the particle-level events located in the same p_T^γ bins at the reconstruction level. The acceptance is dominated by the EM cluster quality selection requirements on $\eta_{\rm det}$, applied to avoid edge effects in the calorimeter regions used for the measurement, and on $\phi_{\rm det}$ in the central rapidity region, applied to avoid periodic calorimeter module boundaries [30] that bias the EM cluster energy and position measurements. The acceptance typically varies within about $1.4-0.8$ with a relative systematic uncertainty of $3\%-12\%$, and takes into account correlation between the same-sign and opposite-sign events. The acceptance greater than unity corresponds to opposite-sign rapidity events with forward jets and low p_T^γ central photons, and are caused by a migration of the (particle-level) same-sign events into the other category. Migration significantly increases the number of reconstructed opposite-sign events due to a much larger cross section for same-sign events at small p_T^γ (see Sec.VI). Correction factors to account for differences between jet-p_T and rapidity spectra in data and simulation are estimated with PYTHIA, and used as weights to create a data-like MC sample. The differences between acceptance corrections obtained with standard and data-like MC samples are taken as a systematic uncertainty of up to 10% at small p_T^γ. An additional systematic uncertainty of up to 7% is assigned from a comparison of the photon selection efficiency calculated with PYTHIA and SHERPA.

Small differences between data and MC in the photon selection efficiencies are corrected using factors derived from $Z \to e^+e^-$ control samples, as well as photons from radiative Z boson decays [37]. The total efficiency of the photon selection criteria is $68\%-80\%$, depending on the p_T^γ and y^γ region. The systematic uncertainties caused by these correction factors are 3% for $|y^\gamma| < 1.0$ and 7.3% for $1.5 < |y^\gamma| < 2.5$ and are mainly due to uncertainties caused by the track-match veto, isolation, and the photon NN requirements.

V. SUMMARY OF SYSTEMATIC UNCERTAINTIES

The main sources of experimental systematic uncertainty on the prompt $\gamma+$jet production cross section in two kinematic regions, $|y^\gamma| < 1.0$, $|y^{\rm jet}| \le 0.8$, $y^\gamma y^{\rm jet} > 0$ and, $1.5 < |y^\gamma| < 2.5$, $2.4 < |y^{\rm jet}| \le 3.2$, $y^\gamma y^{\rm jet} > 0$, are shown, as an example, in Fig. 6. Similar uncertainties are found for the other kinematic regions. The largest uncertainties are assigned to the signal purity estimation ($11\%-3\%$), photon and jet selections ($3\%-10\%$), jet energy scale ($7\%-1\%$), photon energy scale ($3\%-8\%$), EM trigger selection (6% for $20 < p_T^\gamma < 35$ GeV and 1% for $p_T^\gamma \ge 35$ GeV) and the integrated luminosity (6.1%). The uncertainty ranges cover the intervals from low p_T^γ to high p_T^γ. The systematic uncertainty on the photon selection is due to the correction determined by comparing the observed data/MC difference in the efficiency to pass the photon selection criteria, and a reconstruction of the photon production vertex z-position (2% for events with central photons and 6% for forward photons). The total experimental systematic uncertainty for each data point is obtained by adding the individual contributions in quadrature. A common normalization uncertainty of 6.8% for events with central photons and 11.2% for forward photons resulting from uncertainties on integrated luminosity, photon selection efficiency, and photon production vertex selection (see above) is not included in the figures, but is included in the tables. Correlations between systematic uncertainties are given in Ref. [51] to increase the value of these data in future PDF fits. Bin-by-bin correlations in p_T^γ are provided for the seven sources of systematic uncertainty. The normalization uncertainties are not included in those tables.

VI. DIFFERENTIAL CROSS SECTION AND COMPARISON WITH THEORY

The differential cross section $\mathrm{d}^3\sigma/\mathrm{d}p_T^\gamma \mathrm{d}y^\gamma \mathrm{d}y^{\rm jet}$ for $\gamma+$ jet production is obtained from the number of data events in each interval after applying corrections for signal purity, acceptance and efficiency, divided by the integrated luminosity and the widths of the interval in the photon transverse momentum, photon rapidity, and jet rapidity. For all regions we choose intervals of $\mathrm{d}y^\gamma = 2.0$ and $\mathrm{d}y^{\rm jet} = 1.6$.

The cross sections for each region are presented as a function of p_T^γ in Fig. 7. The data points are shown at the value $\langle p_T^\gamma \rangle$ for which a value of a smooth function describing the cross section dependence equals the average cross section in that bin [52]. The cross sections cover 5–6 orders of magnitude in each rapidity range, and fall more rapidly for events with larger jet and/or photon rapidities. The cross section of events with same-sign rapidities has a steeper p_T^γ spectrum than for the opposite-sign events. As an example, in Fig. 8 we show ratios of the same-sign to opposite-sign cross sections for two extreme cases, central photon and central jet, and forward photon and very forward jet. The ratio reaches about a factor of 1.2 at low p_T^γ at central photon and jet rapidities, while for the forward rapidities it varies by up to a factor of 10. In both cases the ratio drops to about unity at high p_T^γ.

The data are compared to next-to-leading order (NLO) perturbative QCD (pQCD) predictions obtained using JETPHOX [28, 29], with CT10 PDF [53] and BFG frag-

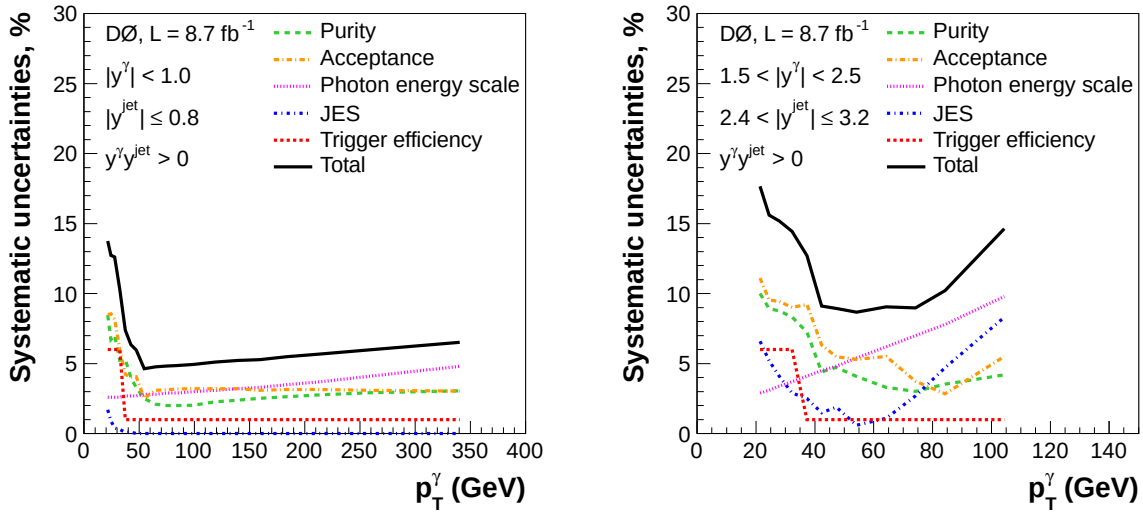

FIG. 6: (color online) Systematic uncertainties on the prompt γ + jet production cross sections for events with central and forward photons (same-sign events with $|y^{\rm jet}| \leq 0.8$ and $2.4 < |y^{\rm jet}| \leq 3.2$ are shown as an example). A common normalization uncertainty of 6.8% for events with central photons and 11.2% for forward photons resulting from integrated luminosity, photon selection efficiency, and photon production vertex are not included in the figures.

mentation functions of partons to photons [54]. The renormalization, factorization, and fragmentation scales (μ_R, μ_F, and μ_f) are set equal to p_T^γ. The uncertainty due to the scale choice is estimated via a simultaneous variation, up and down, by a factor of two of all three scales relative to the central value ($\mu_R = \mu_F = \mu_f = p_T^\gamma$). The CT10 PDF uncertainties are estimated using 26 pairs of eigenvectors following the prescription of Ref. [55].

To compare data to the JETPHOX predictions at the particle level, the latter are corrected for non-perturbative effects caused by (a) parton-to-hadron fragmentation and (b) MPI. These corrections are evaluated using PYTHIA MC samples in two steps: (a) as a ratio of γ+jet cross section after fragmentation to that before fragmentation (i.e., at the parton level) with the MPI effect switched off, and (b) as the ratio of γ+jet cross section after switching on the MPI effect to that without it. The typical size of the correction for the fragmentation effect is about $0.98 - 1.02$ with 1% uncertainty. As the default MPI tune we choose Perugia-0 (P0) [46] since it shows the best description of the azimuthal distributions in γ+2-jet and γ+3-jet events [56]. To estimate a systematic uncertainty due to the MPI effect, other tunes have been considered as well: P-hard and P-soft [46], that explore the dependence on the strength of initial- and final-state radiation effects, while maintaining a roughly consistent MPI model as implemented in the P0 tune; P-nocr, which excludes any color reconnections in the final state; DW [57] with Q^2-ordered showers as an alternative to the P0 tune with p_T-ordered showers. We take asymmetric systematic uncertainties defined as maximal deviations up and down from the central prediction with P0. Generally, they correspond to P-hard and P-soft tunes. The typical size of the correction for the MPI effect is $0.96 - 0.98$ with an uncertainty of $2\% - 5\%$. The overall correction for the non-perturbative effects is applied to the JETPHOX predictions with uncertainties added to the theory scale uncertainty. Tables I–XVI show measured and predicted NLO cross sections with their uncertainties for all sixteen studied regions.

To make a more detailed comparison, the ratio of the measured cross section to the pQCD NLO prediction is calculated in each interval. The results are shown in Figs. 9 and 10. The normalization uncertainty (6.8% for events with central photons and 11.2% for forward photons) are not included in the figures. Ratios of the JETPHOX predictions with MSTW2008NLO [58] and NNPDFv2.1 [59] PDF sets to those with CT10 PDF set are also shown. The results are also compared to the predictions from SHERPA and PYTHIA. The JETPHOX scale uncertainties are $10\% - 15\%$ for events with central photons and jets, but increase to $35\% - 40\%$ for events with forward photons and more forward jets. The CT10 PDF uncertainties usually increase with p_T^γ and may reach $40\% - 50\%$ in some regions of the phase space, e.g., at high p_T^γ with forward photons and either $y^\gamma y^{\rm jet} \leq 0$ and $|y^{\rm jet}| \leq 0.8$, or $y^\gamma y^{\rm jet} > 0$ and $2.4 < |y^{\rm jet}| \leq 3.2$.

For central photons, the pQCD NLO theory agrees with data except for small p_T^γ in almost all jet rapidity regions, and except for high p_T^γ with very forward jets ($2.4 < |y^{\rm jet}| \leq 3.2$) and opposite-sign photon-jet rapidities. Qualitatively, these results are very similar to those obtained by ATLAS Collaboration [26]. Due to small size of the fragmentation photon contribution ($< 10\%$) and a weak dependence of theoretical scale uncertainties on p_T^γ, a possible explanation is the mismodeling of

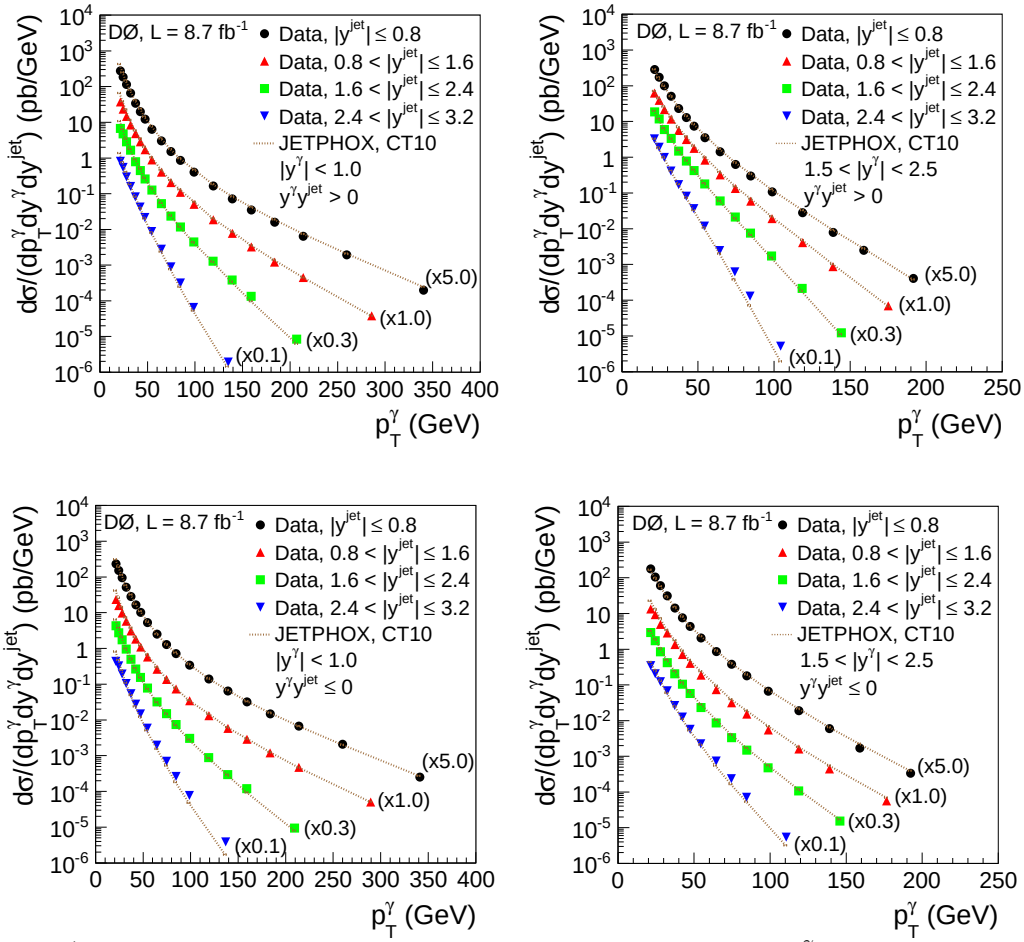

FIG. 7: (color online) The measured differential γ + jet cross section as a function of p_T^{γ} for the four measured jet rapidity intervals, with central photons, $|y^{\gamma}| < 1.0$, and forward photons, $1.5 < |y^{\gamma}| < 2.5$, for same-sign and opposite-sign of photon and jet rapidities. For presentation purposes, cross sections for $|y^{\rm jet}| \leq 0.8$, $0.8 < |y^{\rm jet}| \leq 1.6$, $1.6 < |y^{\rm jet}| \leq 2.4$ and $2.4 < |y^{\rm jet}| \leq 3.2$ are scaled by factors of 5, 1, 0.3 and 0.1, respectively. The data are compared to the NLO QCD predictions using the JETPHOX package [29] with the CT10 PDF set [53] and $\mu_R = \mu_F = \mu_f = p_T^{\gamma}$.

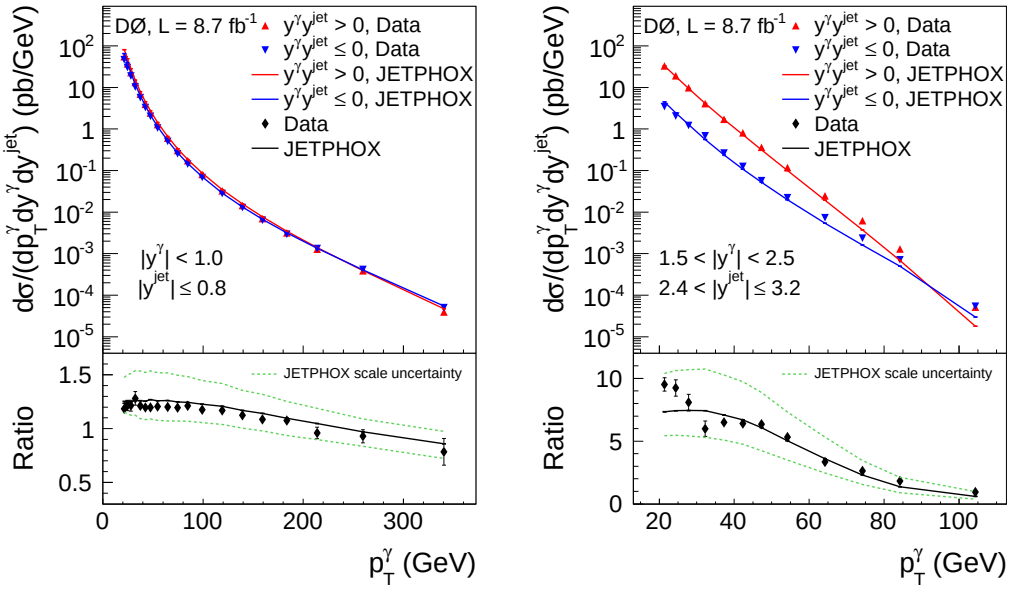

FIG. 8: (color online) Comparison of the same-sign to opposite-sign cross section ratios for events with a central photon and central jet and those with a forward photon and very forward jet.

the gluon PDF. The shapes of cross sections predicted by SHERPA agree with the data but are typically slightly low with a significant exception for events with very forward jets where the SHERPA predictions agree well with data at $20 \leq p_T^\gamma \lesssim 50$ GeV, and are much larger at higher p_T^γ. Predictions from PYTHIA are about a factor of $1.3-2$ below the measured data points. For events with forward photons, the NLO theory agrees with data within theoretical and experimental uncertainties, except for the region $p_T^\gamma > 70$ GeV in the same-sign events with very forward jets.

VII. SUMMARY

The triple differential cross section $\mathrm{d}^3\sigma/\mathrm{d}p_T^\gamma \mathrm{d}y^\gamma \mathrm{d}y^{\mathrm{jet}}$ for the associated inclusive photon and jet production process $p\bar{p} \to \gamma + \mathrm{jet} + X$ is measured for events with central ($|y^\gamma| < 1.0$) and forward ($1.5 < |y^\gamma| < 2.5$) photons in four jet rapidity intervals ($|y^{\mathrm{jet}}| \leq 0.8$, $0.8 < |y^{\mathrm{jet}}| \leq 1.6$, $1.6 < |y^{\mathrm{jet}}| \leq 2.4$, and $2.4 < |y^{\mathrm{jet}}| \leq 3.2$), for configurations with same and for opposite sign of photon and jet rapidities.

The pQCD NLO predictions describe data with central photons in almost all jet rapidity regions except low p_T^γ (< 40 GeV) and the opposite-sign rapidity events at high p_T^γ with very forward jets ($2.4 < |y^{\mathrm{jet}}| < 3.2$). They also describe data with forward photons except for the same-sign rapidity events with $p_T^\gamma > 70$ GeV and $2.4 < |y^{\mathrm{jet}}| \leq 3.2$. The measured cross sections typically have similar or smaller uncertainties than the NLO PDF and scale uncertainties. These measurements provide valuable information for tuning QCD theory predictions and particularly can be used as valuable input to global fits to gluon and other PDFs.

We thank the staffs at Fermilab and collaborating institutions, and acknowledge support from the DOE and NSF (USA); CEA and CNRS/IN2P3 (France); MON, NRC KI and RFBR (Russia); CNPq, FAPERJ, FAPESP and FUNDUNESP (Brazil); DAE and DST (India); Colciencias (Colombia); CONACyT (Mexico); NRF (Korea); FOM (The Netherlands); STFC and the Royal Society (United Kingdom); MSMT and GACR (Czech Republic); BMBF and DFG (Germany); SFI (Ireland); The Swedish Research Council (Sweden); and CAS and CNSF (China).

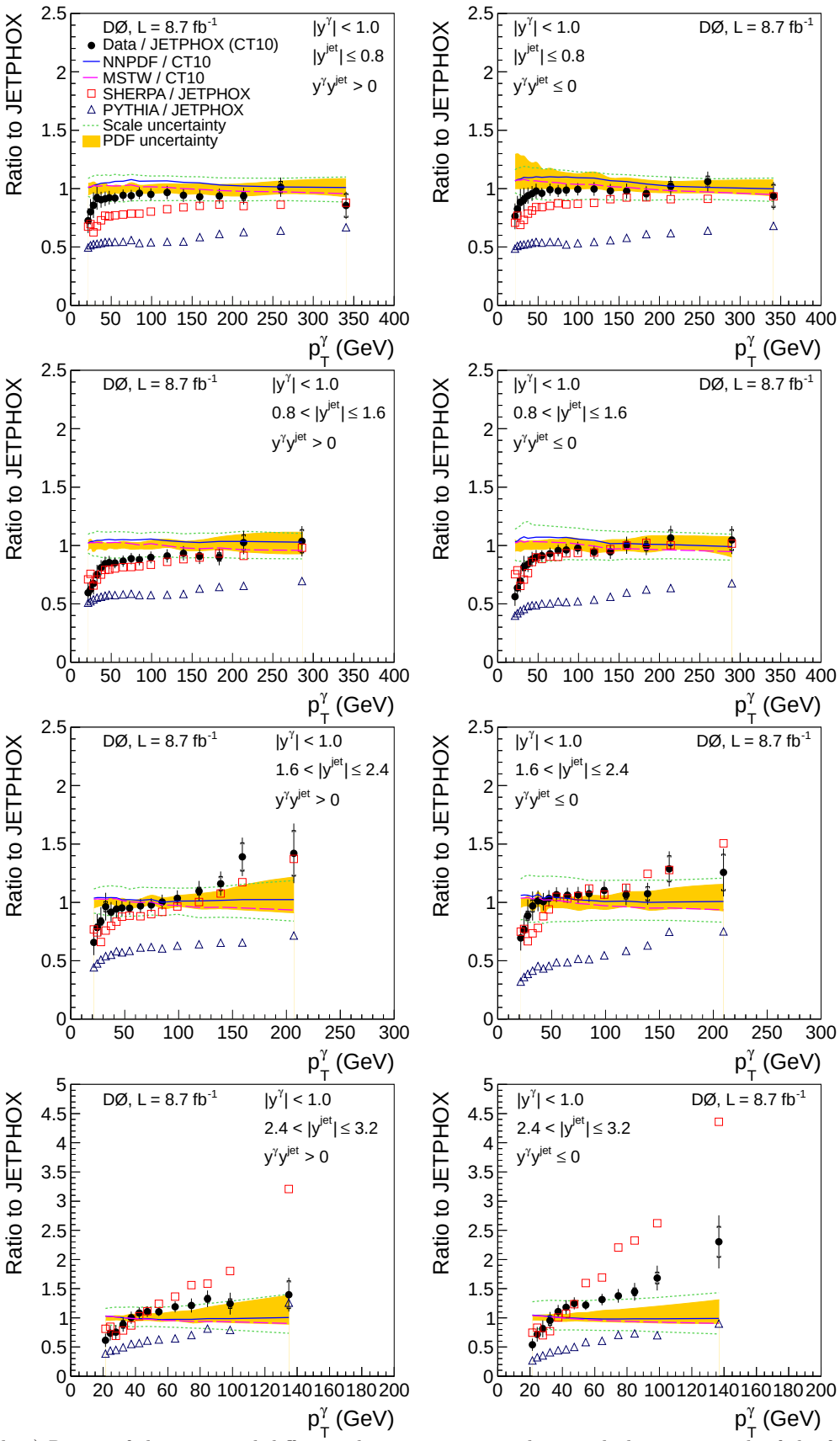

FIG. 9: (color online) Ratios of the measured differential cross sections with central photons in each of the four measured jet rapidity intervals to the pQCD NLO prediction using JETPHOX [29] with the CT10 PDF set and $\mu_R = \mu_F = \mu_f = p_T^\gamma$. The solid vertical line on the points shows the statistical and p_T-dependent systematic uncertainties added in quadrature, while the internal line shows the statistical uncertainty. A common 6.8% normalization uncertainty on the data points is not shown. The two dotted lines represent the effect of varying the theoretical scales of JETPHOX by a factor of two. The shaded region is the CT10 [53] PDF uncertainty. The dashed and dash-dotted lines show ratios of the JETPHOX predictions with MSTW2008NLO [58] and NNPDFv2.1 [59] to CT10 PDF sets. The predictions from SHERPA and PYTHIA are shown by the open squares and triangles, respectively.

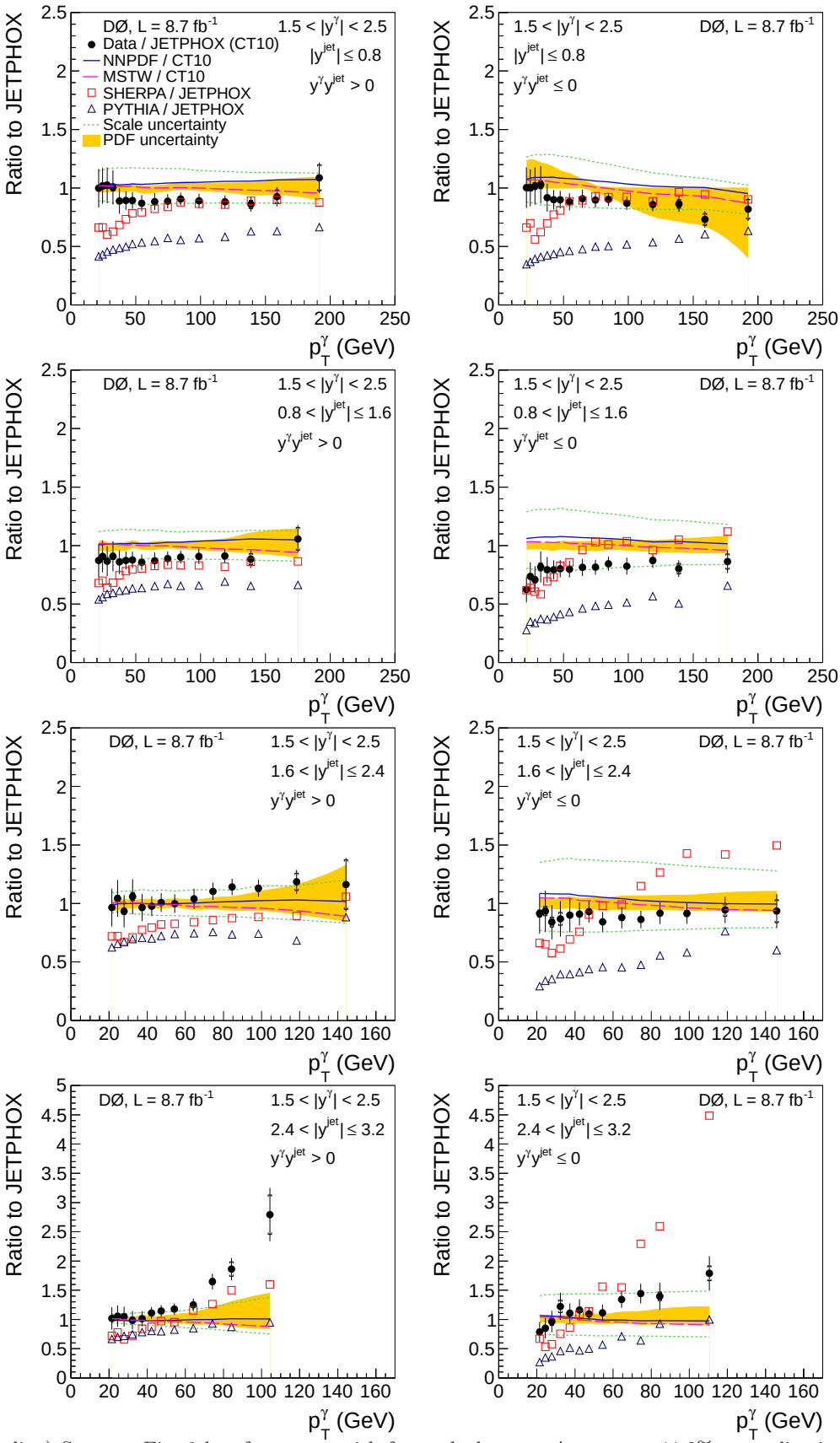

FIG. 10: (color online) Same as Fig. 9 but for events with forward photons. A common 11.2% normalization uncertainty on the data points is not shown.

Appendix: Measured cross sections

TABLE I: The γ + jet cross section $\mathrm{d}^3\sigma/\mathrm{d}p_T^\gamma \mathrm{d}y^\gamma \mathrm{d}y^{\mathrm{jet}}$ in bins of p_T^γ for $|y^\gamma| < 1.0$ and $|y^{\mathrm{jet}}| \leq 0.8$, $y^\gamma y^{\mathrm{jet}} > 0$ together with statistical (δ_{stat}) and systematic (δ_{syst}) uncertainties, and the NLO prediction together with scale (δ_{scale}) and PDF (δ_{pdf}) uncertainties. A common normalization uncertainty of 6.8% is included in δ_{syst} for all points.

p_T^γ bin	$\langle p_T^\gamma \rangle$	$\mathrm{d}^3\sigma/\mathrm{d}p_T^\gamma \mathrm{d}y^\gamma \mathrm{d}y^{\mathrm{jet}}$ (pb/GeV)						
(GeV)	(GeV)	Data	δ_{stat}(%)	δ_{syst}(%)	δ_{tot}(%)	NLO	δ_{scale}(%)	δ_{pdf}(%)
20 – 23	21.4	5.52×10^{1}	2.4	15.3	15.5	7.61×10^{1}	+8.7/ –6.7	+4.6/ –5.4
23 – 26	24.4	3.69×10^{1}	2.7	14.4	14.7	4.61×10^{1}	+9.7/ –7.5	+4.8/ –4.6
26 – 30	27.9	2.30×10^{1}	2.9	14.3	14.6	2.68×10^{1}	+10.9/ –8.3	+5.7/ –3.6
30 – 35	32.3	1.31×10^{1}	3.3	12.4	12.8	1.43×10^{1}	+11.6/ –8.9	+4.0/ –4.3
35 – 40	37.3	6.87×10^{0}	1.3	10.0	10.1	7.60×10^{0}	+11.2/ –10.3	+3.6/ –4.3
40 – 45	42.4	3.96×10^{0}	1.3	9.3	9.4	4.34×10^{0}	+11.8/ –10.4	+4.4/ –2.7
45 – 50	47.4	2.44×10^{0}	1.3	9.0	9.1	2.64×10^{0}	+11.0/ –11.0	+1.8/ –5.2
50 – 60	54.6	1.28×10^{0}	1.3	8.2	8.3	1.39×10^{0}	+12.1/ –10.9	+2.9/ –4.1
60 – 70	64.7	6.03×10^{-1}	1.3	8.3	8.4	6.40×10^{-1}	+11.3/ –11.4	+2.4/ –4.5
70 – 80	74.7	3.05×10^{-1}	1.3	8.3	8.4	3.25×10^{-1}	+12.1/ –10.6	+5.0/ –2.2
80 – 90	84.7	1.73×10^{-1}	1.4	8.4	8.5	1.80×10^{-1}	+11.4/ –10.4	+2.9/ –3.8
90 – 110	99.1	8.04×10^{-2}	1.4	8.4	8.5	8.46×10^{-2}	+10.8/ –10.3	+3.4/ –4.2
110 – 130	119.2	3.27×10^{-2}	1.6	8.5	8.6	3.38×10^{-2}	+10.9/ –10.4	+4.1/ –3.4
130 – 150	139.3	1.44×10^{-2}	1.9	8.6	8.8	1.53×10^{-2}	+10.2/ –10.2	+3.9/ –4.8
150 – 170	159.4	6.95×10^{-3}	2.4	8.6	8.9	7.47×10^{-3}	+10.1/ –10.3	+4.1/ –4.5
170 – 200	183.7	3.16×10^{-3}	2.7	8.7	9.2	3.38×10^{-3}	+9.1/ –10.7	+3.5/ –6.1
200 – 230	213.8	1.28×10^{-3}	4.0	8.9	9.7	1.37×10^{-3}	+9.0/ –10.5	+4.3/ –6.3
230 – 300	259.6	3.88×10^{-4}	4.7	9.1	10.2	3.83×10^{-4}	+8.8/ –10.3	+6.7/ –4.4
300 – 400	340.5	3.95×10^{-5}	11.9	9.4	15.2	4.62×10^{-5}	+10.0/ –11.5	+8.5/ –7.1

TABLE II: Same as in Table I but for $|y^\gamma| < 1.0$ and $0.8 < |y^{\mathrm{jet}}| \leq 1.6$, $y^\gamma y^{\mathrm{jet}} > 0$.

p_T^γ bin	$\langle p_T^\gamma \rangle$	$\mathrm{d}^3\sigma/\mathrm{d}p_T^\gamma \mathrm{d}y^\gamma \mathrm{d}y^{\mathrm{jet}}$ (pb/GeV)						
(GeV)	(GeV)	Data	δ_{stat}(%)	δ_{syst}(%)	δ_{tot}(%)	NLO	δ_{scale}(%)	δ_{pdf}(%)
20 – 23	21.4	3.70×10^{1}	2.4	15.7	15.9	6.22×10^{1}	+9.5/ –6.6	+4.2/ –4.5
23 – 26	24.4	2.32×10^{1}	2.9	15.0	15.2	3.72×10^{1}	+10.9/ –7.9	+5.1/ –2.5
26 – 30	27.9	1.45×10^{1}	3.1	15.2	15.5	2.16×10^{1}	+10.9/ –9.1	+2.5/ –5.1
30 – 35	32.3	8.44×10^{0}	3.7	12.6	13.1	1.13×10^{1}	+12.1/ –9.2	+3.7/ –3.0
35 – 40	37.3	4.79×10^{0}	1.3	10.5	10.6	5.92×10^{0}	+11.7/ –10.3	+3.2/ –3.0
40 – 45	42.4	2.84×10^{0}	1.3	9.7	9.8	3.36×10^{0}	+11.4/ –10.7	+2.1/ –3.9
45 – 50	47.4	1.71×10^{0}	1.3	9.3	9.4	2.01×10^{0}	+11.4/ –10.8	+2.4/ –2.4
50 – 60	54.6	8.87×10^{-1}	1.3	8.4	8.5	1.04×10^{0}	+11.9/ –10.8	+2.4/ –3.0
60 – 70	64.6	4.04×10^{-1}	1.3	8.6	8.7	4.67×10^{-1}	+11.6/ –10.8	+3.5/ –2.2
70 – 80	74.7	2.06×10^{-1}	1.4	8.5	8.6	2.33×10^{-1}	+11.4/ –10.3	+2.7/ –3.2
80 – 90	84.7	1.09×10^{-1}	1.4	8.6	8.7	1.24×10^{-1}	+10.3/ –10.0	+2.6/ –3.0
90 – 110	99.0	5.00×10^{-2}	1.4	8.6	8.7	5.57×10^{-2}	+11.2/ –9.7	+4.4/ –3.1
110 – 130	119.1	1.85×10^{-2}	1.8	8.8	8.9	2.04×10^{-2}	+11.3/ –9.8	+5.4/ –1.8
130 – 150	139.2	7.75×10^{-3}	2.3	9.0	9.3	8.31×10^{-3}	+9.9/ –10.8	+3.7/ –4.2
150 – 170	159.3	3.24×10^{-3}	3.2	9.3	9.8	3.57×10^{-3}	+10.6/ –10.5	+4.6/ –4.5
170 – 200	183.6	1.22×10^{-3}	4.1	9.2	10.1	1.35×10^{-3}	+10.3/ –10.3	+7.4/ –3.5
200 – 230	213.8	4.51×10^{-4}	6.5	9.4	11.5	4.40×10^{-4}	+12.2/ –11.3	+9.6/ –5.6
230 – 400	285.9	3.80×10^{-5}	9.7	10.4	14.2	3.67×10^{-5}	+10.2/ –11.4	+11.4/ –7.1

TABLE III: Same as in Table I but for $|y^{\gamma}| < 1.0$ and $1.6 < |y^{\rm jet}| \leq 2.4$, $y^{\gamma} y^{\rm jet} > 0$.

p_T^{γ} bin	$\langle p_T^{\gamma} \rangle$	$\mathrm{d}^3\sigma/\mathrm{d}p_T^{\gamma}\mathrm{d}y^{\gamma}\mathrm{d}y^{\rm jet}$ (pb/GeV)						
(GeV)	(GeV)	Data	$\delta_{\rm stat}$(%)	$\delta_{\rm syst}$(%)	$\delta_{\rm tot}$(%)	NLO	$\delta_{\rm scale}$(%)	$\delta_{\rm pdf}$(%)
20 – 23	21.4	2.26×10^{1}	2.9	17.0	17.3	3.43×10^{1}	+11.6/ –9.3	+1.8/ –4.7
23 – 26	24.4	1.58×10^{1}	3.4	15.3	15.7	2.01×10^{1}	+12.3/ –9.7	+1.7/ –3.8
26 – 30	27.9	9.45×10^{0}	3.8	15.7	16.1	1.13×10^{1}	+13.4/ –10.3	+2.4/ –3.0
30 – 35	32.3	5.52×10^{0}	4.6	13.1	13.9	5.73×10^{0}	+13.8/ –11.2	+2.1/ –3.4
35 – 40	37.3	2.63×10^{0}	1.3	11.6	11.7	2.88×10^{0}	+14.2/ –11.4	+3.9/ –1.3
40 – 45	42.4	1.48×10^{0}	1.3	10.1	10.1	1.57×10^{0}	+13.7/ –11.7	+2.7/ –3.4
45 – 50	47.4	8.61×10^{-1}	1.3	9.8	9.9	9.05×10^{-1}	+13.5/ –12.1	+3.4/ –2.1
50 – 60	54.5	4.23×10^{-1}	1.3	9.0	9.1	4.45×10^{-1}	+11.4/ –11.9	+1.4/ –4.3
60 – 70	64.6	1.76×10^{-1}	1.4	9.1	9.2	1.82×10^{-1}	+13.0/ –11.7	+3.1/ –4.0
70 – 80	74.6	7.89×10^{-2}	1.5	9.0	9.1	8.07×10^{-2}	+12.7/ –10.9	+6.0/ –2.1
80 – 90	84.7	3.87×10^{-2}	1.8	9.2	9.4	3.86×10^{-2}	+12.5/ –11.5	+4.0/ –5.3
90 – 110	98.8	1.48×10^{-2}	1.9	9.5	9.7	1.43×10^{-2}	+12.1/ –10.3	+5.9/ –3.7
110 – 130	118.9	4.28×10^{-3}	3.0	10.1	10.6	3.91×10^{-3}	+12.3/ –13.2	+7.5/ –5.7
130 – 150	139.0	1.28×10^{-3}	5.3	10.3	11.5	1.10×10^{-3}	+13.5/ –12.7	+10.1/ –5.5
150 – 170	159.1	4.45×10^{-4}	8.7	10.9	14.0	3.20×10^{-4}	+15.5/ –13.2	+14.7/ –6.5
170 – 300	206.9	2.82×10^{-5}	13.7	14.3	19.8	1.98×10^{-5}	+18.7/ –16.1	+21.6/ –9.0

TABLE IV: Same as in Table I but for $|y^{\gamma}| < 1.0$ and $2.4 < |y^{\rm jet}| \leq 3.2$, $y^{\gamma} y^{\rm jet} > 0$.

p_T^{γ} bin	$\langle p_T^{\gamma} \rangle$	$\mathrm{d}^3\sigma/\mathrm{d}p_T^{\gamma}\mathrm{d}y^{\gamma}\mathrm{d}y^{\rm jet}$ (pb/GeV)						
(GeV)	(GeV)	Data	$\delta_{\rm stat}$(%)	$\delta_{\rm syst}$(%)	$\delta_{\rm tot}$(%)	NLO	$\delta_{\rm scale}$(%)	$\delta_{\rm pdf}$(%)
20 – 23	21.4	8.09×10^{0}	3.9	19.0	19.4	1.32×10^{1}	+16.1/ –11.8	+3.4/ –3.8
23 – 26	24.4	5.44×10^{0}	4.9	16.6	17.3	7.40×10^{0}	+17.4/ –12.6	+2.8/ –4.4
26 – 30	27.9	2.95×10^{0}	6.0	16.8	17.9	3.91×10^{0}	+18.3/ –13.7	+3.7/ –3.7
30 – 35	32.3	1.61×10^{0}	7.5	13.7	15.6	1.81×10^{0}	+18.1/ –13.8	+3.4/ –4.7
35 – 40	37.3	8.15×10^{-1}	1.4	12.2	12.3	8.13×10^{-1}	+18.7/ –15.3	+6.4/ –5.4
40 – 45	42.3	4.22×10^{-1}	1.4	11.2	11.2	3.89×10^{-1}	+18.1/ –15.1	+4.5/ –4.9
45 – 50	47.3	2.16×10^{-1}	1.4	10.4	10.5	1.95×10^{-1}	+18.5/ –14.9	+6.8/ –4.4
50 – 60	54.5	8.67×10^{-2}	1.5	9.7	9.9	7.86×10^{-2}	+18.3/ –15.4	+7.5/ –6.0
60 – 70	64.5	2.78×10^{-2}	1.9	10.5	10.7	2.34×10^{-2}	+19.2/ –16.4	+10.8/ –5.4
70 – 80	74.6	8.96×10^{-3}	2.7	11.0	11.3	7.39×10^{-3}	+21.4/ –17.6	+12.7/ –8.8
80 – 90	84.6	3.17×10^{-3}	4.3	12.6	13.3	2.39×10^{-3}	+24.4/ –18.6	+18.2/ –7.1
90 – 110	98.5	6.47×10^{-4}	6.6	15.7	17.1	5.20×10^{-4}	+28.5/ –20.7	+24.7/ –8.2
110 – 200	134.9	1.93×10^{-5}	17.1	14.7	22.5	1.38×10^{-5}	+40.6/ –26.6	+38.6/ –11.0

TABLE V: Same as in Table I but for $|y^\gamma| < 1.0$ and $|y^{\rm jet}| \leq 0.8$, $y^\gamma y^{\rm jet} \leq 0$.

p_T^γ bin	$\langle p_T^\gamma \rangle$	$\mathrm{d}^3\sigma/\mathrm{d}p_T^\gamma \mathrm{d}y^\gamma \mathrm{d}y^{\rm jet}$ (pb/GeV)						
(GeV)	(GeV)	Data	$\delta_{\rm stat}$(%)	$\delta_{\rm syst}$(%)	$\delta_{\rm tot}$(%)	NLO	$\delta_{\rm scale}$(%)	$\delta_{\rm pdf}$(%)
20 – 23	21.4	4.66×10^{1}	2.4	15.2	15.4	6.11×10^{1}	+16.2/ –3.6	+29.1/ –0.0
23 – 26	24.4	3.04×10^{1}	2.8	14.4	14.7	3.69×10^{1}	+17.6/ –4.7	+29.8/ –0.0
26 – 30	27.9	1.89×10^{1}	3.0	14.5	14.8	2.14×10^{1}	+18.0/ –5.5	+28.2/ –0.0
30 – 35	32.3	1.02×10^{1}	3.6	12.3	12.8	1.13×10^{1}	+18.9/ –6.0	+27.8/ –0.0
35 – 40	37.3	5.67×10^{0}	1.3	9.9	10.0	6.03×10^{0}	+18.6/ –8.4	+24.0/ –0.0
40 – 45	42.4	3.31×10^{0}	1.3	9.3	9.4	3.46×10^{0}	+17.6/ –8.9	+22.0/ –0.0
45 – 50	47.4	2.04×10^{0}	1.3	9.1	9.2	2.08×10^{0}	+17.8/ –9.0	+22.6/ –0.0
50 – 60	54.6	1.06×10^{0}	1.3	8.2	8.3	1.11×10^{0}	+16.9/ –9.5	+16.7/ –0.0
60 – 70	64.7	5.03×10^{-1}	1.3	8.3	8.4	5.08×10^{-1}	+16.9/ –9.8	+17.4/ –0.0
70 – 80	74.7	2.55×10^{-1}	1.4	8.3	8.4	2.60×10^{-1}	+16.0/ –9.5	+14.7/ –0.0
80 – 90	84.7	1.43×10^{-1}	1.4	8.3	8.4	1.45×10^{-1}	+15.6/ –9.5	+13.6/ –0.2
90 – 110	99.1	6.84×10^{-2}	1.4	8.3	8.4	6.89×10^{-2}	+14.2/ –9.4	+12.8/ –0.4
110 – 130	119.2	2.79×10^{-2}	1.6	8.4	8.6	2.80×10^{-2}	+13.8/ –9.3	+14.2/ –0.0
130 – 150	139.3	1.28×10^{-2}	2.0	8.5	8.7	1.31×10^{-2}	+12.3/ –9.7	+9.0/ –1.8
150 – 170	159.4	6.40×10^{-3}	2.4	8.6	8.9	6.55×10^{-3}	+11.9/ –9.7	+9.2/ –1.8
170 – 200	183.8	2.95×10^{-3}	2.8	8.7	9.1	3.08×10^{-3}	+10.7/ –10.0	+7.2/ –3.1
200 – 230	213.9	1.34×10^{-3}	3.9	8.8	9.6	1.31×10^{-3}	+9.9/ –9.5	+6.1/ –3.7
230 – 300	259.8	4.18×10^{-4}	4.6	9.0	10.1	3.95×10^{-4}	+8.4/ –9.3	+6.9/ –3.8
300 – 400	341.1	5.04×10^{-5}	10.5	9.6	14.2	5.38×10^{-5}	+8.9/ –11.0	+7.5/ –6.2

TABLE VI: Same as in Table I but for $|y^\gamma| < 1.0$ and $0.8 < |y^{\rm jet}| \leq 1.6$, $y^\gamma y^{\rm jet} \leq 0$.

p_T^γ bin	$\langle p_T^\gamma \rangle$	$\mathrm{d}^3\sigma/\mathrm{d}p_T^\gamma \mathrm{d}y^\gamma \mathrm{d}y^{\rm jet}$ (pb/GeV)						
(GeV)	(GeV)	Data	$\delta_{\rm stat}$(%)	$\delta_{\rm syst}$(%)	$\delta_{\rm tot}$(%)	NLO	$\delta_{\rm scale}$(%)	$\delta_{\rm pdf}$(%)
20 – 23	21.4	2.34×10^{1}	2.5	15.2	15.4	4.17×10^{1}	+14.0/ –12.4	+5.0/ –5.0
23 – 26	24.4	1.57×10^{1}	3.0	15.2	15.5	2.47×10^{1}	+15.0/ –13.7	+3.6/ –4.6
26 – 30	27.9	9.71×10^{0}	3.3	15.4	15.7	1.39×10^{1}	+17.0/ –13.6	+4.4/ –5.1
30 – 35	32.3	5.81×10^{0}	4.0	12.7	13.3	7.12×10^{0}	+20.0/ –13.2	+3.6/ –3.5
35 – 40	37.3	3.08×10^{0}	1.3	10.2	10.3	3.67×10^{0}	+20.4/ –13.8	+3.7/ –3.4
40 – 45	42.4	1.81×10^{0}	1.3	9.6	9.7	2.05×10^{0}	+17.7/ –14.0	+4.0/ –3.5
45 – 50	47.4	1.10×10^{0}	1.3	9.2	9.3	1.22×10^{0}	+17.4/ –13.8	+4.1/ –3.1
50 – 60	54.6	5.73×10^{-1}	1.3	8.4	8.5	6.29×10^{-1}	+17.3/ –13.8	+4.4/ –3.4
60 – 70	64.6	2.62×10^{-1}	1.3	8.4	8.5	2.81×10^{-1}	+16.5/ –13.5	+5.2/ –2.7
70 – 80	74.7	1.35×10^{-1}	1.4	8.4	8.5	1.41×10^{-1}	+16.0/ –13.1	+5.0/ –3.7
80 – 90	84.7	7.33×10^{-2}	1.5	8.4	8.5	7.62×10^{-2}	+15.5/ –12.0	+6.8/ –2.8
90 – 110	99.0	3.46×10^{-2}	1.5	8.5	8.6	3.54×10^{-2}	+14.9/ –12.4	+5.7/ –4.0
110 – 130	119.2	1.32×10^{-2}	1.9	8.6	8.8	1.40×10^{-2}	+13.0/ –12.2	+3.3/ –6.1
130 – 150	139.3	5.76×10^{-3}	2.5	8.7	9.0	6.09×10^{-3}	+12.4/ –12.8	+4.9/ –5.1
150 – 170	159.4	2.86×10^{-3}	3.3	8.9	9.5	2.85×10^{-3}	+11.7/ –11.7	+5.3/ –4.6
170 – 200	183.7	1.20×10^{-3}	4.1	9.0	9.9	1.20×10^{-3}	+12.2/ –11.8	+8.0/ –5.7
200 – 230	213.9	4.69×10^{-4}	6.4	9.5	11.5	4.41×10^{-4}	+11.4/ –11.3	+8.3/ –3.5
230 – 400	289.5	5.02×10^{-5}	8.6	9.6	12.9	4.80×10^{-5}	+9.6/ –12.7	+7.2/ –9.8

TABLE VII: Same as in Table I but for $|y^\gamma| < 1.0$ and $1.6 < |y^{\rm jet}| \leq 2.4$, $y^\gamma y^{\rm jet} \leq 0$.

p_T^γ bin	$\langle p_T^\gamma \rangle$	$\mathrm{d}^3\sigma/\mathrm{d}p_T^\gamma \mathrm{d}y^\gamma \mathrm{d}y^{\rm jet}$ (pb/GeV)						
(GeV)	(GeV)	Data	$\delta_{\rm stat}$(%)	$\delta_{\rm syst}$(%)	$\delta_{\rm tot}$(%)	NLO	$\delta_{\rm scale}$(%)	$\delta_{\rm pdf}$(%)
20 – 23	21.4	1.44×10^{1}	3.1	16.6	16.9	2.07×10^{1}	+20.1/ –15.0	+3.1/ –4.4
23 – 26	24.4	9.11×10^{0}	3.9	15.8	16.2	1.19×10^{1}	+22.1/ –14.6	+3.7/ –3.2
26 – 30	27.9	5.85×10^{0}	4.3	16.4	16.9	6.61×10^{0}	+23.3/ –16.8	+5.4/ –3.1
30 – 35	32.3	3.19×10^{0}	5.4	13.2	14.3	3.30×10^{0}	+22.7/ –17.3	+1.4/ –7.1
35 – 40	37.3	1.65×10^{0}	1.4	10.9	11.0	1.62×10^{0}	+22.3/ –16.5	+8.7/ –3.4
40 – 45	42.4	8.87×10^{-1}	1.3	9.9	10.0	8.82×10^{-1}	+22.4/ –18.2	+3.3/ –9.2
45 – 50	47.4	5.15×10^{-1}	1.3	9.5	9.6	4.99×10^{-1}	+22.4/ –16.9	+3.5/ –4.8
50 – 60	54.5	2.60×10^{-1}	1.3	9.0	9.1	2.44×10^{-1}	+22.2/ –16.6	+4.3/ –4.6
60 – 70	64.6	1.07×10^{-1}	1.4	9.1	9.2	1.01×10^{-1}	+21.5/ –16.4	+4.9/ –5.1
70 – 80	74.7	4.98×10^{-2}	1.6	9.3	9.4	4.68×10^{-2}	+20.4/ –16.4	+4.3/ –6.8
80 – 90	84.7	2.46×10^{-2}	1.9	9.4	9.6	2.29×10^{-2}	+18.6/ –15.7	+5.9/ –5.4
90 – 110	98.9	1.01×10^{-2}	2.1	9.5	9.7	9.15×10^{-3}	+18.8/ –15.4	+5.7/ –6.0
110 – 130	119.0	2.95×10^{-3}	3.4	9.7	10.3	2.77×10^{-3}	+19.0/ –15.2	+8.9/ –3.8
130 – 150	139.1	9.77×10^{-4}	5.6	9.7	11.2	9.10×10^{-4}	+19.0/ –15.5	+9.3/ –6.8
150 – 170	159.2	3.97×10^{-4}	8.7	10.5	13.6	3.09×10^{-4}	+19.0/ –15.4	+11.8/ –5.7
170 – 300	209.4	3.14×10^{-5}	12.4	13.0	18.0	2.50×10^{-5}	+20.8/ –17.0	+15.4/ –7.3

TABLE VIII: Same as in Table I but for $|y^\gamma| < 1.0$ and $2.4 < |y^{\rm jet}| \leq 3.2$, $y^\gamma y^{\rm jet} \leq 0$.

p_T^γ bin	$\langle p_T^\gamma \rangle$	$\mathrm{d}^3\sigma/\mathrm{d}p_T^\gamma \mathrm{d}y^\gamma \mathrm{d}y^{\rm jet}$ (pb/GeV)						
(GeV)	(GeV)	Data	$\delta_{\rm stat}$(%)	$\delta_{\rm syst}$(%)	$\delta_{\rm tot}$(%)	NLO	$\delta_{\rm scale}$(%)	$\delta_{\rm pdf}$(%)
20 – 23	21.4	4.38×10^{0}	4.4	18.8	19.3	8.14×10^{0}	+27.6/ –18.4	+4.3/ –3.8
23 – 26	24.4	3.25×10^{0}	5.5	17.1	18.0	4.52×10^{0}	+28.4/ –19.0	+4.7/ –4.0
26 – 30	27.8	1.93×10^{0}	6.6	16.9	18.2	2.38×10^{0}	+29.5/ –19.7	+4.9/ –4.2
30 – 35	32.3	1.04×10^{0}	8.8	13.6	16.2	1.09×10^{0}	+30.1/ –20.0	+5.5/ –4.8
35 – 40	37.3	5.38×10^{-1}	1.4	11.6	11.7	4.85×10^{-1}	+29.6/ –21.1	+6.1/ –5.7
40 – 45	42.3	2.75×10^{-1}	1.4	12.1	12.2	2.33×10^{-1}	+29.2/ –20.6	+6.1/ –6.0
45 – 50	47.3	1.47×10^{-1}	1.5	10.3	10.4	1.18×10^{-1}	+29.5/ –20.8	+8.2/ –5.3
50 – 60	54.5	5.89×10^{-2}	1.5	9.2	9.3	4.84×10^{-2}	+29.4/ –21.2	+9.2/ –6.0
60 – 70	64.5	1.97×10^{-2}	2.0	9.8	10.0	1.50×10^{-2}	+30.9/ –21.6	+12.5/ –6.7
70 – 80	74.6	7.00×10^{-3}	3.0	10.7	11.1	5.09×10^{-3}	+31.2/ –21.8	+14.0/ –7.4
80 – 90	84.6	2.61×10^{-3}	4.5	11.5	12.3	1.81×10^{-3}	+32.4/ –22.4	+16.5/ –7.8
90 – 110	98.6	7.66×10^{-4}	6.0	11.5	12.9	4.55×10^{-4}	+34.9/ –23.9	+20.2/ –9.0
110 – 200	136.8	3.87×10^{-5}	11.5	13.2	17.5	1.68×10^{-5}	+43.0/ –27.6	+31.0/ –9.6

TABLE IX: The γ + jet cross section $\mathrm{d}^3\sigma/\mathrm{d}p_T^\gamma \mathrm{d}y^\gamma \mathrm{d}y^{\mathrm{jet}}$ in bins of p_T^γ for $1.5 < |y^\gamma| < 2.5$ and $|y^{\mathrm{jet}}| \leq 0.8$, $y^\gamma y^{\mathrm{jet}} > 0$ together with statistical (δ_{stat}) and systematic (δ_{syst}) uncertainties, and the NLO prediction together with scale (δ_{scale}) and PDF (δ_{pdf}) uncertainties. A common normalization uncertainty of 11.2% is included in δ_{syst} for all points.

p_T^γ bin	$\langle p_T^\gamma \rangle$	$\mathrm{d}^3\sigma/\mathrm{d}p_T^\gamma \mathrm{d}y^\gamma \mathrm{d}y^{\mathrm{jet}}$ (pb/GeV)						
(GeV)	(GeV)	Data	δ_{stat}(%)	δ_{syst}(%)	δ_{tot}(%)	NLO	δ_{scale}(%)	δ_{pdf}(%)
20 – 23	21.4	5.67×10^{1}	2.2	18.2	18.4	5.69×10^{1}	+14.5/ −11.0	+4.3/ −3.9
23 – 26	24.4	3.46×10^{1}	2.5	17.0	17.1	3.41×10^{1}	+15.4/ −11.2	+3.8/ −3.4
26 – 30	27.9	2.00×10^{1}	2.6	16.9	17.1	1.96×10^{1}	+16.5/ −11.8	+2.6/ −3.4
30 – 35	32.3	1.02×10^{1}	3.0	16.6	16.9	1.01×10^{1}	+17.0/ −13.0	+3.5/ −2.7
35 – 40	37.3	4.64×10^{0}	1.3	15.0	15.0	5.23×10^{0}	+17.2/ −13.2	+2.5/ −3.1
40 – 45	42.4	2.56×10^{0}	1.2	12.3	12.3	2.87×10^{0}	+17.0/ −13.4	+2.3/ −3.4
45 – 50	47.4	1.47×10^{0}	1.3	11.8	11.9	1.65×10^{0}	+17.4/ −13.9	+3.6/ −2.5
50 – 60	54.6	7.00×10^{-1}	1.2	11.7	11.8	8.05×10^{-1}	+16.8/ −14.0	+1.8/ −4.4
60 – 70	64.6	2.86×10^{-1}	1.3	11.8	11.8	3.24×10^{-1}	+16.8/ −14.1	+2.0/ −3.8
70 – 80	74.6	1.26×10^{-1}	1.4	10.9	11.0	1.42×10^{-1}	+16.5/ −13.3	+3.0/ −2.4
80 – 90	84.7	5.94×10^{-2}	1.4	10.6	10.7	6.55×10^{-2}	+16.6/ −13.2	+5.0/ −1.3
90 – 110	98.8	2.14×10^{-2}	1.5	11.2	11.3	2.41×10^{-2}	+14.9/ −13.1	+4.0/ −2.3
110 – 130	118.8	5.64×10^{-3}	2.2	11.0	11.2	6.39×10^{-3}	+14.0/ −12.8	+4.3/ −3.7
130 – 150	138.9	1.57×10^{-3}	4.1	11.3	12.1	1.82×10^{-3}	+13.3/ −13.1	+4.6/ −5.9
150 – 170	158.9	5.00×10^{-4}	6.4	11.8	13.4	5.41×10^{-4}	+13.3/ −12.7	+7.1/ −5.6
170 – 230	191.6	8.15×10^{-5}	10.3	12.4	16.1	7.51×10^{-5}	+12.6/ −13.2	+9.2/ −10.8

TABLE X: Same as in Table IX but of p_T^γ for $1.5 < |y^\gamma| < 2.5$ and $0.8 < |y^{\mathrm{jet}}| \leq 1.6$, $y^\gamma y^{\mathrm{jet}} > 0$.

p_T^γ bin	$\langle p_T^\gamma \rangle$	$\mathrm{d}^3\sigma/\mathrm{d}p_T^\gamma \mathrm{d}y^\gamma \mathrm{d}y^{\mathrm{jet}}$ (pb/GeV)						
(GeV)	(GeV)	Data	δ_{stat}(%)	δ_{syst}(%)	δ_{tot}(%)	NLO	δ_{scale}(%)	δ_{pdf}(%)
20 – 23	21.4	6.20×10^{1}	2.1	18.2	18.4	7.12×10^{1}	+11.8/ −8.4	+3.5/ −4.6
23 – 26	24.4	3.89×10^{1}	2.3	16.9	17.1	4.29×10^{1}	+12.2/ −8.7	+3.6/ −3.9
26 – 30	27.9	2.13×10^{1}	2.5	16.8	17.0	2.46×10^{1}	+13.0/ −9.5	+2.6/ −4.8
30 – 35	32.3	1.16×10^{1}	2.9	16.4	16.6	1.28×10^{1}	+12.8/ −10.7	+2.2/ −4.5
35 – 40	37.3	5.61×10^{0}	1.3	14.8	14.9	6.53×10^{0}	+13.5/ −11.0	+2.5/ −3.9
40 – 45	42.3	3.11×10^{0}	1.2	12.3	12.4	3.56×10^{0}	+13.8/ −11.1	+2.7/ −4.0
45 – 50	47.4	1.78×10^{0}	1.3	11.9	11.9	2.02×10^{0}	+13.9/ −11.7	+3.9/ −2.0
50 – 60	54.5	8.27×10^{-1}	1.2	11.8	11.8	9.65×10^{-1}	+12.8/ −11.6	+2.1/ −3.4
60 – 70	64.6	3.22×10^{-1}	1.3	11.9	11.9	3.70×10^{-1}	+13.6/ −11.0	+3.4/ −3.3
70 – 80	74.6	1.34×10^{-1}	1.4	11.1	11.2	1.51×10^{-1}	+12.0/ −11.7	+3.4/ −2.1
80 – 90	84.6	5.91×10^{-2}	1.5	10.8	10.9	6.55×10^{-2}	+11.7/ −11.6	+3.5/ −2.8
90 – 110	98.6	1.92×10^{-2}	1.5	11.5	11.6	2.11×10^{-2}	+12.1/ −11.6	+4.2/ −3.5
110 – 130	118.8	4.09×10^{-3}	2.6	11.3	11.5	4.49×10^{-3}	+11.9/ −12.0	+5.9/ −4.9
130 – 150	138.8	8.66×10^{-4}	5.4	12.0	13.2	9.80×10^{-4}	+12.9/ −12.4	+10.8/ −6.2
150 – 230	175.1	6.97×10^{-5}	9.2	12.3	15.4	6.59×10^{-5}	+12.5/ −13.4	+14.0/ −10.2

TABLE XI: Same as in Table IX but for $1.5 < |y^\gamma| < 2.5$ and $1.6 < |y^{\rm jet}| \leq 2.4$, $y^\gamma y^{\rm jet} > 0$.

p_T^γ bin	$\langle p_T^\gamma \rangle$	$\mathrm{d}^3\sigma/\mathrm{d}p_T^\gamma \mathrm{d}y^\gamma \mathrm{d}y^{\rm jet}$ (pb/GeV)						
(GeV)	(GeV)	Data	$\delta_{\rm stat}(\%)$	$\delta_{\rm syst}(\%)$	$\delta_{\rm tot}(\%)$	NLO	$\delta_{\rm scale}(\%)$	$\delta_{\rm pdf}(\%)$
20 – 23	21.4	6.17×10^{1}	2.3	18.2	18.3	6.40×10^{1}	+9.2/ –8.2	+2.5/ –5.4
23 – 26	24.4	3.92×10^{1}	2.6	16.7	16.9	3.76×10^{1}	+9.7/ –7.3	+2.2/ –5.6
26 – 30	27.9	1.98×10^{1}	2.9	16.7	17.0	2.12×10^{1}	+10.6/ –7.8	+3.4/ –3.8
30 – 35	32.3	1.12×10^{1}	3.3	16.3	16.6	1.06×10^{1}	+10.6/ –9.0	+2.6/ –3.9
35 – 40	37.3	4.96×10^{0}	1.3	14.8	14.9	5.14×10^{0}	+11.8/ –9.1	+3.5/ –2.9
40 – 45	42.3	2.60×10^{0}	1.2	12.3	12.4	2.67×10^{0}	+11.0/ –10.1	+3.2/ –4.0
45 – 50	47.4	1.42×10^{0}	1.3	11.9	12.0	1.41×10^{0}	+11.4/ –10.5	+2.9/ –3.9
50 – 60	54.5	6.00×10^{-1}	1.2	12.0	12.1	6.01×10^{-1}	+10.8/ –10.4	+4.0/ –3.3
60 – 70	64.5	2.00×10^{-1}	1.3	12.2	12.3	1.93×10^{-1}	+11.5/ –11.1	+2.8/ –5.2
70 – 80	74.5	7.03×10^{-2}	1.5	11.3	11.4	6.37×10^{-2}	+11.7/ –11.0	+4.9/ –4.6
80 – 90	84.6	2.49×10^{-2}	1.9	11.1	11.3	2.19×10^{-2}	+11.4/ –11.4	+6.0/ –5.8
90 – 110	98.4	5.72×10^{-3}	2.4	11.6	11.9	5.06×10^{-3}	+14.8/ –12.4	+10.4/ –6.0
110 – 130	118.4	7.10×10^{-4}	6.2	12.2	13.7	5.99×10^{-4}	+15.2/ –14.0	+16.8/ –9.6
130 – 170	144.3	4.08×10^{-5}	18.2	13.2	22.5	3.52×10^{-5}	+19.9/ –16.7	+32.7/ –15.4

TABLE XII: Same as in Table IX but for $1.5 < |y^\gamma| < 2.5$ and $2.4 < |y^{\rm jet}| \leq 3.2$, $y^\gamma y^{\rm jet} > 0$.

p_T^γ bin	$\langle p_T^\gamma \rangle$	$\mathrm{d}^3\sigma/\mathrm{d}p_T^\gamma \mathrm{d}y^\gamma \mathrm{d}y^{\rm jet}$ (pb/GeV)						
(GeV)	(GeV)	Data	$\delta_{\rm stat}(\%)$	$\delta_{\rm syst}(\%)$	$\delta_{\rm tot}(\%)$	NLO	$\delta_{\rm scale}(\%)$	$\delta_{\rm pdf}(\%)$
20 – 23	21.4	3.29×10^{1}	2.9	19.8	20.1	3.23×10^{1}	+8.6/ –5.9	+3.7/ –3.8
23 – 26	24.4	1.90×10^{1}	3.4	18.0	18.4	1.80×10^{1}	+9.8/ –6.1	+7.1/ –2.0
26 – 30	27.9	9.87×10^{0}	3.9	17.7	18.1	9.42×10^{0}	+10.2/ –7.3	+5.1/ –3.4
30 – 35	32.3	4.09×10^{0}	5.3	17.1	17.9	4.14×10^{0}	+10.5/ –9.1	+3.7/ –4.5
35 – 40	37.3	1.71×10^{0}	1.3	15.6	15.7	1.69×10^{0}	+12.1/ –8.9	+7.5/ –2.7
40 – 45	42.3	8.11×10^{-1}	1.3	12.8	12.9	7.30×10^{-1}	+11.6/ –10.3	+4.0/ –5.7
45 – 50	47.3	3.64×10^{-1}	1.3	12.7	12.8	3.18×10^{-1}	+12.7/ –11.8	+5.9/ –5.8
50 – 60	54.2	1.19×10^{-1}	1.3	12.5	12.6	1.01×10^{-1}	+13.5/ –12.6	+8.3/ –5.9
60 – 70	64.2	2.47×10^{-2}	1.8	12.8	12.9	1.97×10^{-2}	+17.2/ –15.0	+12.9/ –8.2
70 – 80	74.2	6.23×10^{-3}	3.3	12.8	13.2	3.78×10^{-3}	+21.6/ –16.8	+21.1/ –7.9
80 – 90	84.2	1.30×10^{-3}	6.7	13.7	15.2	6.98×10^{-4}	+27.5/ –20.2	+30.9/ –11.9
90 – 170	104.4	5.15×10^{-5}	12.0	17.2	21.0	1.84×10^{-5}	+37.8/ –25.0	+45.0/ –15.7

TABLE XIII: Same as in Table IX but for $1.5 < |y^\gamma| < 2.5$ and $|y^{\rm jet}| \leq 0.8$, $y^\gamma y^{\rm jet} \leq 0$.

p_T^γ bin	$\langle p_T^\gamma \rangle$	$\mathrm{d}^3\sigma/\mathrm{d}p_T^\gamma \mathrm{d}y^\gamma \mathrm{d}y^{\rm jet}$ (pb/GeV)						
(GeV)	(GeV)	Data	$\delta_{\rm stat}(\%)$	$\delta_{\rm syst}(\%)$	$\delta_{\rm tot}(\%)$	NLO	$\delta_{\rm scale}(\%)$	$\delta_{\rm pdf}(\%)$
20 – 23	21.4	3.57×10^{1}	2.3	18.8	18.9	3.56×10^{1}	+26.3/ –12.0	+23.2/ –0.0
23 – 26	24.4	2.11×10^{1}	2.7	17.4	17.6	2.11×10^{1}	+27.5/ –12.5	+24.3/ –0.0
26 – 30	27.9	1.22×10^{1}	2.9	17.4	17.6	1.20×10^{1}	+28.5/ –12.9	+23.5/ –0.0
30 – 35	32.3	6.29×10^{0}	3.4	17.3	17.7	6.12×10^{0}	+28.2/ –14.4	+21.4/ –0.0
35 – 40	37.3	2.84×10^{0}	1.3	15.6	15.7	3.09×10^{0}	+28.7/ –14.6	+20.2/ –0.0
40 – 45	42.4	1.51×10^{0}	1.2	12.6	12.7	1.68×10^{0}	+28.4/ –15.0	+17.8/ –0.0
45 – 50	47.4	8.72×10^{-1}	1.3	12.0	12.0	9.68×10^{-1}	+27.2/ –16.0	+14.7/ –0.0
50 – 60	54.5	4.14×10^{-1}	1.2	12.0	12.1	4.69×10^{-1}	+26.6/ –15.9	+12.3/ –0.0
60 – 70	64.6	1.72×10^{-1}	1.3	12.1	12.2	1.90×10^{-1}	+24.4/ –16.3	+7.0/ –0.1
70 – 80	74.6	7.57×10^{-2}	1.4	11.2	11.3	8.45×10^{-2}	+22.1/ –16.9	+2.0/ –3.6
80 – 90	84.7	3.62×10^{-2}	1.5	10.6	10.7	4.01×10^{-2}	+20.4/ –17.3	+0.7/ –7.3
90 – 110	98.8	1.34×10^{-2}	1.5	11.0	11.1	1.53×10^{-2}	+17.1/ –17.8	+0.0/ –15.5
110 – 130	118.9	3.80×10^{-3}	2.3	11.0	11.2	4.42×10^{-3}	+13.0/ –18.3	+0.0/ –24.5
130 – 150	139.0	1.20×10^{-3}	4.2	11.4	12.2	1.39×10^{-3}	+10.3/ –18.2	+0.0/ –28.8
150 – 170	159.0	3.40×10^{-4}	7.0	11.8	13.7	4.65×10^{-4}	+8.2/ –18.4	+0.0/ –33.1
170 – 230	192.4	6.69×10^{-5}	10.2	12.2	16.0	8.17×10^{-5}	+2.4/ –22.3	+0.0/ –59.8

TABLE XIV: Same as in Table IX but for $1.5 < |y^\gamma| < 2.5$ and $0.8 < |y^{\rm jet}| \leq 1.6$, $y^\gamma y^{\rm jet} \leq 0$.

p_T^γ bin	$\langle p_T^\gamma \rangle$	$\mathrm{d}^3\sigma/\mathrm{d}p_T^\gamma \mathrm{d}y^\gamma \mathrm{d}y^{\rm jet}$ (pb/GeV)						
(GeV)	(GeV)	Data	$\delta_{\rm stat}$(%)	$\delta_{\rm syst}$(%)	$\delta_{\rm tot}$(%)	NLO	$\delta_{\rm scale}$(%)	$\delta_{\rm pdf}$(%)
20 – 23	21.4	1.34×10^{1}	2.6	19.2	19.4	2.15×10^{1}	+28.7/ –19.5	+2.9/ –3.3
23 – 26	24.4	9.24×10^{0}	3.1	17.9	18.1	1.26×10^{1}	+29.7/ –19.9	+2.7/ –3.0
26 – 30	27.9	4.94×10^{0}	3.5	17.8	18.1	6.99×10^{0}	+30.5/ –20.4	+2.9/ –2.9
30 – 35	32.3	2.83×10^{0}	4.1	17.8	18.2	3.46×10^{0}	+30.9/ –21.3	+2.4/ –3.0
35 – 40	37.3	1.35×10^{0}	1.3	16.1	16.2	1.70×10^{0}	+31.0/ –21.4	+2.5/ –3.5
40 – 45	42.4	7.11×10^{-1}	1.3	13.0	13.0	8.98×10^{-1}	+30.8/ –21.6	+2.4/ –4.2
45 – 50	47.4	4.00×10^{-1}	1.3	12.6	12.6	4.99×10^{-1}	+31.9/ –21.7	+3.5/ –2.8
50 – 60	54.5	1.87×10^{-1}	1.2	12.4	12.5	2.34×10^{-1}	+30.5/ –21.2	+3.5/ –3.6
60 – 70	64.6	7.40×10^{-2}	1.3	12.4	12.5	9.09×10^{-2}	+29.6/ –20.8	+3.5/ –3.9
70 – 80	74.6	3.18×10^{-2}	1.5	11.7	11.8	3.90×10^{-2}	+28.2/ –20.3	+3.9/ –4.4
80 – 90	84.7	1.51×10^{-2}	1.7	11.2	11.3	1.79×10^{-2}	+27.4/ –19.5	+5.1/ –3.3
90 – 110	98.8	5.45×10^{-3}	1.8	12.5	12.6	6.62×10^{-3}	+25.5/ –18.3	+4.8/ –4.0
110 – 130	118.9	1.60×10^{-3}	2.9	11.3	11.7	1.83×10^{-3}	+22.2/ –17.7	+4.4/ –5.2
130 – 150	138.9	4.39×10^{-4}	5.6	11.7	13.0	5.47×10^{-4}	+21.5/ –16.4	+5.6/ –5.8
150 – 230	176.6	5.65×10^{-5}	7.6	13.1	15.1	6.55×10^{-5}	+18.0/ –16.3	+8.1/ –6.5

TABLE XV: Same as in Table IX but for $1.5 < |y^\gamma| < 2.5$ and $1.6 < |y^{\rm jet}| \leq 2.4$, $y^\gamma y^{\rm jet} \leq 0$.

p_T^γ bin	$\langle p_T^\gamma \rangle$	$\mathrm{d}^3\sigma/\mathrm{d}p_T^\gamma \mathrm{d}y^\gamma \mathrm{d}y^{\rm jet}$ (pb/GeV)						
(GeV)	(GeV)	Data	$\delta_{\rm stat}$(%)	$\delta_{\rm syst}$(%)	$\delta_{\rm tot}$(%)	NLO	$\delta_{\rm scale}$(%)	$\delta_{\rm pdf}$(%)
20 – 23	21.4	9.79×10^{0}	3.4	20.4	20.7	1.07×10^{1}	+35.2/ –23.1	+3.9/ –3.1
23 – 26	24.4	5.79×10^{0}	4.2	19.1	19.6	6.19×10^{0}	+36.0/ –23.8	+3.4/ –3.8
26 – 30	27.9	2.84×10^{0}	4.9	18.6	19.3	3.38×10^{0}	+36.5/ –23.7	+3.8/ –4.2
30 – 35	32.3	1.40×10^{0}	6.4	18.2	19.3	1.61×10^{0}	+37.9/ –24.5	+4.4/ –4.6
35 – 40	37.3	6.81×10^{-1}	1.3	17.4	17.5	7.56×10^{-1}	+38.7/ –24.1	+5.6/ –3.6
40 – 45	42.3	3.50×10^{-1}	1.3	13.7	13.7	3.85×10^{-1}	+37.0/ –24.7	+4.4/ –4.8
45 – 50	47.4	1.91×10^{-1}	1.3	12.9	13.0	2.06×10^{-1}	+37.4/ –24.5	+4.9/ –4.6
50 – 60	54.5	7.73×10^{-2}	1.3	13.3	13.4	9.17×10^{-2}	+36.4/ –24.5	+4.6/ –5.5
60 – 70	64.6	2.88×10^{-2}	1.5	13.5	13.6	3.27×10^{-2}	+36.0/ –23.9	+6.2/ –5.0
70 – 80	74.6	1.11×10^{-2}	1.8	12.1	12.3	1.29×10^{-2}	+35.5/ –23.3	+6.5/ –5.4
80 – 90	84.6	4.96×10^{-3}	2.4	13.3	13.5	5.41×10^{-3}	+34.0/ –22.7	+6.7/ –5.1
90 – 110	98.7	1.59×10^{-3}	2.8	13.0	13.3	1.74×10^{-3}	+32.2/ –22.2	+7.1/ –6.0
110 – 130	118.8	3.54×10^{-4}	5.7	14.0	15.1	3.76×10^{-4}	+30.3/ –21.0	+9.3/ –6.2
130 – 170	145.8	5.09×10^{-5}	10.5	16.1	19.2	5.46×10^{-5}	+27.9/ –20.9	+10.3/ –7.0

TABLE XVI: Same as in Table IX but for $1.5 < |y^\gamma| < 2.5$ and $2.4 < |y^{\rm jet}| \leq 3.2$, $y^\gamma y^{\rm jet} \leq 0$.

p_T^γ bin	$\langle p_T^\gamma \rangle$	$\mathrm{d}^3\sigma/\mathrm{d}p_T^\gamma \mathrm{d}y^\gamma \mathrm{d}y^{\rm jet}$ (pb/GeV)						
(GeV)	(GeV)	Data	$\delta_{\rm stat}$(%)	$\delta_{\rm syst}$(%)	$\delta_{\rm tot}$(%)	NLO	$\delta_{\rm scale}$(%)	$\delta_{\rm pdf}$(%)
20 – 23	21.4	3.45×10^{0}	4.8	23.3	23.8	4.40×10^{0}	+41.0/ –25.3	+4.7/ –5.5
23 – 26	24.4	2.06×10^{0}	6.1	22.4	23.3	2.42×10^{0}	+42.0/ –25.6	+7.0/ –4.6
26 – 30	27.9	1.22×10^{0}	6.9	21.7	22.7	1.27×10^{0}	+42.6/ –26.2	+5.5/ –5.8
30 – 35	32.3	6.82×10^{-1}	8.8	19.8	21.7	5.58×10^{-1}	+43.4/ –26.9	+7.1/ –5.3
35 – 40	37.3	2.64×10^{-1}	1.3	18.4	18.5	2.39×10^{-1}	+43.3/ –26.8	+7.3/ –6.5
40 – 45	42.3	1.26×10^{-1}	1.4	17.9	18.0	1.09×10^{-1}	+43.8/ –27.2	+7.9/ –6.2
45 – 50	47.3	5.73×10^{-2}	1.5	14.8	14.9	5.23×10^{-2}	+44.4/ –27.8	+9.1/ –6.3
50 – 60	54.4	2.23×10^{-2}	1.5	16.3	16.3	2.00×10^{-2}	+43.3/ –28.2	+8.9/ –7.7
60 – 70	64.5	7.36×10^{-3}	2.1	13.9	14.1	5.49×10^{-3}	+45.1/ –27.9	+12.6/ –6.3
70 – 80	74.5	2.36×10^{-3}	3.2	15.0	15.3	1.64×10^{-3}	+44.9/ –28.3	+13.9/ –8.6
80 – 90	84.5	7.09×10^{-4}	5.2	17.6	18.4	5.08×10^{-4}	+46.9/ –28.6	+17.9/ –7.4
90 – 170	110.5	5.45×10^{-5}	7.0	17.9	19.2	3.05×10^{-5}	+48.6/ –29.9	+21.5/ –9.4

[1] J. Alitti *et al.* (UA2 Collaboration), Phys. Lett. B **263**, 544 (1991).
[2] D. Acosta *et al.* (CDF Collaboration), Phys. Rev. D **65**, 112003 (2002).
[3] B. Abbott *et al.* (D0 Collaboration), Phys. Rev. Lett. **84**, 2786 (2000); V. M. Abazov *et al.* (D0 Collaboration), Phys. Rev. Lett. **87**, 2518 (2001).
[4] V. M. Abazov *et al.* (D0 Collaboration), Phys. Lett. B **639**, 151 (2006); V. M. Abazov *et al.* (D0 Collaboration), Phys. Lett. B **658**, 285 (2007).
[5] G. Aad *et al.* (ATLAS Collaboration), Phys. Lett. B **706** (2011) 150.
[6] S. Chatrchyan *et al.* (CMS Collaboration), Phys. Rev. Lett. **106**, 082001 (2011).
[7] P. Aurenche and J. Lindfors, Nucl. Phys. **B168**, 296 (1980); P. Aurenche *et al.*, Phys. Lett. B **140**, 87 (1984); P. Aurenche *et al.*, Zeit. Phys. C **29**, 423 (1985).
[8] J. F. Owens, Rev. Mod. Phys. **59**, 465 (1987).
[9] A. P. Contogouris, N. Mebarki, E. N. Argyres, and S. D. P. Vlassopulos, Phys. Rev. D **35**, 1584 (1987).
[10] P. Aurenche *et al.*, Phys. Rev. D **39**, 3275 (1989).
[11] W. Vogelsang and A. Vogt, Nucl. Phys. **B453**, 334 (1995).
[12] A. D. Martin *et al.*, Eur. Phys. J. C **4**, 463 (1998).
[13] D. V. Bandurin and N. B. Skachkov, Phys. Part. Nucl. **35**, 66 (2004).
[14] E. L. Berger and J. W. Qiu, Phys. Lett. B **248**, 371 (1990).
[15] The polar angle θ is defined with respect to the positive z axis, which is along the proton beam direction, while the azimuthal angle ϕ is defined with respect to the x axis. Rapidity is related to the polar scattering angle θ by $y = 0.5\ln[(1+\beta\cos\theta)/(1-\beta\cos\theta)]$, with $\beta = |\vec{p}|/E$. Also, $|\eta_{\rm det}| = -\ln[\tan(\theta_{\rm det}/2)]$ and $|\phi_{\rm det}|$ are the pseudorapidity and the azimuthal angle defined with respect to the geometric center of the D0 detector.
[16] T. Sjöstrand, S. Mrenna, and P. Z. Skands, J. High Energy Phys. **05**, 026 (2006). We use PYTHIA version v6.420.
[17] P. Nadolsky *et al.*, Phys. Rev. D **78**, 013004 (2008).
[18] T. Akesson *et al.* (ISR–AFS Collaboration), Zeit. Phys. C **34**, 293 (1987).
[19] J. Alitti *et al.* (UA2 Collaboration), Phys. Lett. B **299**, 174 (1993).
[20] A. Aktas *et al.* (H1 Collaboration), Eur. Phys. J. C **38**, 437 (2005).
[21] F. D. Aaron *et al.* (H1 Collaboration), Eur. Phys. J. C **54**, 371 (2008).
[22] S. Chekanov *et al.* (ZEUS Collaboration), Phys. Lett. B **595**, 86 (2004).
[23] S. Chekanov *et al.* (ZEUS Collaboration), Eur. Phys. J. C **49**, 511 (2007).
[24] F. Abe *et al.* (CDF Collaboration), Phys. Rev. D **57**, 67 (1998).
[25] V. M. Abazov *et al.* (D0 Collaboration), Phys. Lett. B **666**, 435 (2008).
[26] G. Aad *et al.* (ATLAS Collaboration), Phys. Rev. D **85**, 092014 (2012).
[27] P. Aurenche *et al.*, Phys. Rev. D **73**, 094007 (2006).
[28] P. Aurenche *et al.*, Nucl. Phys. B **297**, 661 (1988); F. Aversa *et al.*, Nucl. Phys. B **327**, 105 (1989).
[29] S. Catani *et al.*, J. High Energy Phys. **05**, 028 (2002).
[30] V. M. Abazov *et al.* (D0 Collaboration), Nucl. Instrum. Methods Phys. Res. A **565**, 463 (2006).
[31] M. Abolins *et al.*, Nucl. Instrum. Methods in Phys. Res. Sect. A **584**, 75 (2008).
[32] R. Angstadt *et al.*, Nucl. Instrum. Methods in Phys. Res. Sect. A **622**, 298 (2010).
[33] T. Andeen *et al.*, FERMILAB-TM-2365 (2007).
[34] V. M. Abazov *et al.* (D0 Collaboration), Phys. Lett. B **659**, 856 (2008).
[35] V. M. Abazov *et al.* (D0 Collaboration), Phys. Rev. Lett. **102**, 231801 (2009).
[36] R. Brun and F. Carminati, CERN Program Library Long Writeup W5013, 1993 (unpublished).
[37] V. M. Abazov *et al.* (D0 Collaboration), Phys. Rev. D **85**, 052001 (2012).
[38] V. M. Abazov *et al.* (D0 Collaboration), Phys. Lett. B **690**, 108 (2010).
[39] V. M. Abazov *et al.* (D0 Collaboration), accepted for publication in Phys. Rev. D, arXiv:1301.5358.
[40] G. C. Blazey *et al.*, arXiv:hep-ex/0005012 (2000).
[41] V. M. Abazov *et al.* (D0 Collaboration), Nucl. Instrum. Methods Phys. in preparation.
[42] T. Gleisberg *et al.*, J. High Energy Phys. **02**, 007 (2009). We use SHERPA version v1.3.1.
[43] R. Field and R. Craig Group, arXiv:hep-ph/0510198.
[44] S. Höche, S. Schumann, and F. Siegert, Phys. Rev. D **81**, 034026 (2010). As suggested by the SHERPA authors, we choose $Q_{\rm cut} = 10$ GeV as the ME-PS matching scale and the parameter $D = 0.4$ taken to be of the size of the photon isolation cone.
[45] T. Sjöstrand and P. Z. Skands, Eur. Phys. J. C **39**, 129 (2005).
[46] P. Z. Skands, Fermilab-CONF-09-113-T, arXiv:0905.3418 [hep-ph].
[47] S. Catani *et al.*, J. High Energy Phys. **11**, 063 (2001).
[48] C. Buttar *et al.*, arXiv:0803.0678 [hep-ph], section 9.
[49] M. L. Mangano *et al.*, J. High Energy Phys. **07**, 1 (2003). We use ALPGEN version v2.11_d0_wcfix.
[50] R. J. Barlow and C. Beeston, Comp. Phys. Comm. **77**, 219 (1993).
[51] See EPAPS Document No. E-PRILTAO-xxx. For more information on EPAPS, see `http://aip.org/pubservs/epaps.html`.
[52] G. D. Lafferty and T. R. Wyatt, Nucl. Instrum. Meth. Phys. Res. A **355**, 541 (1995).
[53] H. L. Lai, *et al.*, Phys.Rev. D **82**, 074024 (2010).
[54] L. Bourhis, M. Fontannaz, and J. P. Guillet, Eur. Phys. J. C **2**, 529 (1998).
[55] P. Nadolsky and Z. Sullivan, eConf C010630 (2001) P510, hep-ph/0110378.
[56] V. M. Abazov *et al.* (D0 Collaboration), Phys. Rev. D **83**, 052008 (2011).
[57] M. G. Albrow *et al.*, TeV4LHC QCD Working Group, arXiv:hep-ph/0610012.
[58] A. D. Martin *et al.*, Eur. Phys. J. C **63**, 189 (2009).
[59] R. D. Ball *et al.*, Nucl. Phys. B **849**, 296 (2011).